

RESEARCH ARTICLE

Dual spring force couples yield multifunctionality and ultrafast, precision rotation in tiny biomechanical systems

Gregory P. Sutton^{1,‡}, Ryan St Pierre^{2,‡}, Chi-Yun Kuo^{3,*}, Adam P. Summers⁴, Sarah Bergbreiter⁵, Suzanne Cox³ and S. N. Patek^{3,‡,§}

ABSTRACT

Small organisms use propulsive springs rather than muscles to repeatedly actuate high acceleration movements, even when constrained to tiny displacements and limited by inertial forces. Through integration of a large kinematic dataset, measurements of elastic recoil, energetic math modeling and dynamic math modeling, we tested how trap-jaw ants (Odontomachus brunneus) utilize multiple elastic structures to develop ultrafast and precise mandible rotations at small scales. We found that O. brunneus develops torque on each mandible using an intriguing configuration of two springs: their elastic head capsule recoils to push and the recoiling muscleapodeme unit tugs on each mandible. Mandibles achieved precise, planar, circular trajectories up to 49,100 rad s⁻¹ (470,000 rpm) when powered by spring propulsion. Once spring propulsion ended, the mandibles moved with unconstrained and oscillatory rotation. We term this mechanism a 'dual spring force couple', meaning that two springs deliver energy at two locations to develop torque. Dynamic modeling revealed that dual spring force couples reduce the need for joint constraints and thereby reduce dissipative joint losses, which is essential to the repeated use of ultrafast, small systems. Dual spring force couples enable multifunctionality: trap-jaw ants use the same mechanical system to produce ultrafast, planar strikes driven by propulsive springs and for generating slow, multi-degrees of freedom mandible manipulations using muscles, rather than springs, to directly actuate the movement. Dual spring force couples are found in other systems and are likely widespread in biology. These principles can be incorporated into microrobotics to improve multifunctionality, precision and longevity of ultrafast systems.

KEY WORDS: Biomechanics, Springs, Elastic recoil, Fast movement, Control, Trap-jaw ants, Dynamics

INTRODUCTION

In terms of high acceleration, small size and long-term repeated use, biological performance currently exceeds that of synthetic systems.

¹School of Life Sciences, University of Lincoln, Lincoln LN6 7TS, UK. ²Department of Mechanical and Aerospace Engineering, University at Buffalo, Buffalo, NY 14260, USA. ³Biology Department, Duke University, Durham, NC 27708, USA ⁴Friday Harbor Laboratories, University of Washington, Friday Harbor, WA 98250, USA. ⁵Department of Mechanical Engineering, Carnegie Mellon University, Pittsburgh, PA 15213, USA

*Present address: Department of Biomedical & Environmental Biology, Kaohsiung Medical University, Kaohsiung 807, Taiwan.

§Author for correspondence (snp2@duke.edu)

8533-9358; A.P.S., 0000-0003-1930-9748; S.B., 0000-0003-2735-0206; S.C., 0000-0002-9704-0716; S.N.P., 0000-0001-9738-882X

DG.P.S., 0000-0002-3099-9842; R.S., 0000-0003-4609-5642; C.-Y.K., 0000-0002-

The combined capabilities of extreme acceleration and the ability to repeatedly use the system without immediate failure are achieved through latch-mediated spring actuation (LaMSA). LaMSA mechanisms actuate movement primarily using stored elastic energy, which is mediated by latch mechanisms (Bennet-Clark, 1975; Gronenberg, 1996; Galantis and Woledge, 2003; Patek et al., 2011; Ilton et al., 2018; Bolmin et al., 2019; Longo et al., 2019; Bolmin et al., 2021). Many organisms use LaMSA to generate high acceleration movements thousands of times to locomote or strike with minimal reduction in performance. In small, ultrafast systems, spring actuation is more effective than motor-driven movement because of energetic limits and the scaling of elastic energy storage and delivery (Rosario et al., 2016; Ilton et al., 2018, 2019; Sutton et al., 2019). However, with decreasing size, joint dissipative forces – such as friction, viscosity and adhesion - begin to exceed Newtonian forces (Trimmer, 1989; Scherge, 2001; Dai et al., 2006), ultimately restricting rotational rate (Garcia et al., 2000). A triad of remarkable performance – ultrafast movement, elastic actuation and small joints – is evident in biological systems, but has not yet been achieved in synthetic systems. This sets the stage for the central question of this study: how is elastic energy stored and delivered to actuate small, precise, fast-rotating systems? We answer this question using new empirical datasets of trap-jaw ant elastic mechanisms and mandible strikes integrated with dynamic math modeling to yield general physical principles for small, ultrafast, spring-driven systems (Figs 1 and 2).

Most studies establish the presence of actuation with springs by using a mathematical inference approach termed power amplification (Alexander and Bennet-Clark, 1977; Roberts and Azizi, 2011), whereas how springs actually generate movement, especially the actuation of the prevalent joint-based rotational movements of animals, remains largely unresolved (Longo et al., 2019). Yet, many LaMSA systems use multiple or distributed springs (Rosario and Patek, 2015), and this is often manifested as the combined deformation of exoskeletal structures and stretching of internal structures, such as muscle-apodeme units (Burrows et al., 2008; Longo et al., 2021). Recoiling stiff cuticular structures launch flea jumps (Bennet-Clark and Lucey, 1967), froghopper jumps (Burrows et al., 2008) and mantis shrimp predatory strikes (Patek et al., 2013; Rosario and Patek, 2015). Recoiling tendons or tendon-like structures enhance frog jumps (Astley and Roberts, 2014) and galago jumps (Aerts, 1998). Combined recoil of tendon-like structures and hard cuticular structures powers locust jumps (Bennet-Clark, 1975) and predatory strikes of the dragonfly nymph (Büsse et al., 2021). The spatial and temporal scales of ultrafast spring-based propulsion are nearly invisible with even the most advanced imaging systems and often require creative alternative approaches to capture the system's overall energetics (Ilton et al., 2019; Kuan et al., 2020; Bolmin et al., 2021; Jorge et al., 2021). Elastic recoil can be incredibly brief, as evidenced in the 0.1 µs recoil propelling enidarian stinging cells (nematocysts) (Nüchter et al., 2006).





Fig. 1. Trap-jaw ant mandibles. Trap-jaw ants use large mandibles to capture and process prey either using slow, muscle-driven contractions that allow multi-degrees of freedom rotations of their mandibles or by switching to a configuration using a latch-mediated spring actuation (LaMSA) system that produces rapid rotation of the mandibles driven solely by recoiling springs. (A) Trap-jaw ants in the genus *Odontomachus* (*O. bauri* shown here) can strike prey using extremely high angular velocities of their mandibles. These ultrafast strikes are driven by stored elastic energy and released using a latch; this individual has cocked and latched its mandibles prior to an ultrafast strike. (B) Trap-jaw ants can also use their mandibles more slowly – driven directly by muscle contractions (not stored elastic energy) – as multi-degrees of freedom tools to pick up and process prey. Images [©]Alex Wild, used with permission.

To establish how multi-spring propulsion generates extreme rotational movement, it is necessary to consider how the delivery of elastic recoil energy both enables and is limited by joint mechanics. Issues related to complex and deformable joint morphologies, high rotation rates and reduction of energetic losses have been considered extensively in biological and synthetic insect flight systems (Miyan et al., 1985; Walker et al., 2012; Lau et al., 2014; Walker et al., 2014; Mountcastle et al., 2019; Gau et al., 2021). In insect flight, for instance, the thorax flexes to cyclically store and release elastic energy and indirectly actuate wing rotation at rates of 600–6000 rad s⁻¹ (Hedenström, 2014); the joint articulation of the wing is a substantial source of energetic losses (Dudley, 2000; Gau et al., 2019). However, elastic actuation of insect wings relies on efficient, energetic return and oscillatory dynamics, with indirect actuation and relatively low power density of the elastic mechanism (8.6±2.4 W kg⁻¹) (Gau et al., 2019). In contrast, LaMSA systems typically generate a single, high acceleration movement which is directly actuated with high mechanical power density elastic structures. For instance, small arthropod joints leverage milligram and microgram masses at extremely high angular velocities, including leg joints in grasshoppers (300 rad s⁻¹) (Bennet-Clark, 1975), gearing systems in planthoppers (3000 rad s⁻¹) (Burrows and Sutton, 2013), mandible strikes in termites (150,000 rad s⁻¹) (Dickinson, 2006; Kuan et al., 2020) and striking appendages in mantis shrimp (5000 rad s⁻¹) (McHenry et al., 2016). Higher angular velocities in LaMSA systems generate larger inertial reaction forces acting on the system, increasing the risk of catastrophic failure.

Therefore, generating a single ultrafast, repeated-use (i.e. not self-destructing) movement imposes mechanical trade-offs faced to a lesser extent by less power dense and slower oscillatory mechanisms. Extremely fast movements could reduce the joint degrees of freedom to avoid catastrophic failure. However, constrained joint mechanics is accompanied by energetic losses in

these tiny systems. For instance, at these scales, a pin joint reduces degrees of freedom but also introduces substantial frictional forces (Contreras and Pister, 2016). Further, given that ultrafast movement at these scales is often driven by the mechanical transformation of stored elastic potential energy to rotational kinetic energy, the resolution of these constraints must occur while using high energy density elastic structures; the small sizes of these systems do not accommodate large displacements for storing substantial elastic potential energy (i.e. work=force×distance; distance is highly limited in tiny, pre-loaded elastic systems). As LaMSA systems succeed in generating repeatable, precise, extremely fast motions at these scales, analysis of their mechanisms can illuminate general principles circumventing these constraints and trade-offs.

We tested how organisms navigate this intersection of elastic actuation and joint constraints by studying one of the fastest rotating, repeated-use movements vet discovered - trap-jaw ant mandible strikes (Fig. 1). Trap-jaw ants directly actuate their mandibles with springs to drive ultrafast rotations: they deform stiff cuticular structures (the head capsule) and tendon-like structures (mandible adductor muscle and associated apodeme) (Gronenberg, 1995a,b; Patek et al., 2006; Spagna et al., 2008; Larabee et al., 2017; Larabee et al., 2018; Matsuda et al., 2020). When using LaMSA, they latch their mandibles in place and then contract muscles in the head to store elastic energy through deformation of both the head capsule and muscle-apodeme unit (apodeme is the arthropod equivalent of a tendon) (Fig. 1A). They then un-latch their mandibles, at which point the release of the stored elastic energy drives the fast, circular mandible rotation. Trap-jaw ants perform mandible strikes dozens of times in succession without visible damage to the mandibles or head.

To our knowledge, the mechanism by which stored elastic energy in the head and apodeme is transformed into the rotational kinetic energy of the mandible strike has yet to be established. Previous morphological studies of the *Odontomachus* trap-jaw mandible

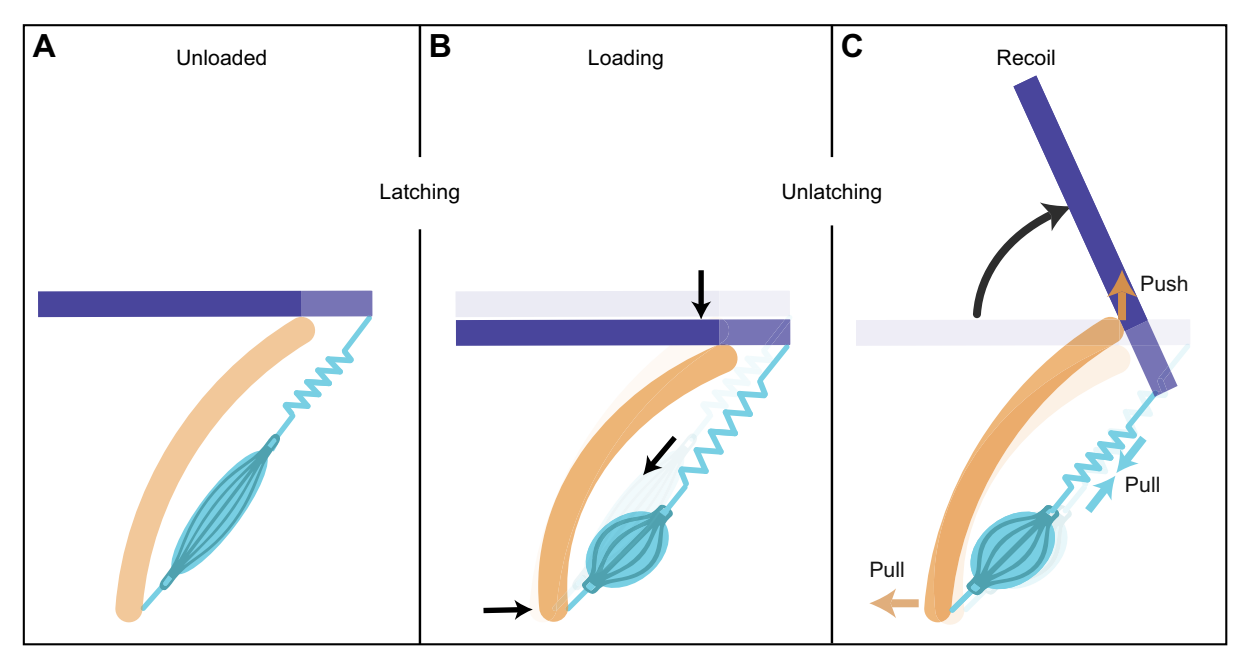


Fig. 2. A general model for a dual spring force couple found in trap-jaw ants that propels their ultrafast mandible snaps. When their LaMSA system is activated, trap-jaw ants use a dual spring force couple, defined as two springs working in tandem to generate a moment. (A) The adductor muscle and apodeme (teal) connects to the mandible (purple) and the interior of the head capsule (orange). This is the configuration used for muscle-driven movement – when there is no latching and spring loading. Dorsal view: anterior is toward the top of the page; lateral is to the left of the page. Only one mandible and a lateral portion of the head capsule are illustrated. (B) When latched, the contraction of the adductor muscle strains (i.e. stretches) the apodeme and deflects the head capsule. This muscle contraction causes the anterior portion of the head to move posteriorly (downward vertical arrow) and a lateral portion of the head to move medially (right-pointing horizontal arrow). (C) After unlatching, the head capsule recoils to assume its original shape. The recoil causes the anterior portion of the head to push on the joint (orange vertical arrow), while the lateral portion of the head pulls on the posterior section of the muscle—apodeme unit (orange horizontal arrow). The pull from the side of the head is transmitted through the recoiling (i.e. re-shortening) muscle and apodeme (teal arrows) to the end of the mandible. The dual spring push and pull generates a force couple that rotates the mandible.

joint were conducted when the head was in the relaxed state (i.e. not spring loaded); in this state, the mandibles attach externally to the head with the ventral extension/protrusion of the mandible base free to move in and out of the head as part of a hypothesized latch mechanism (Gronenberg, 1995a,b). When their LaMSA mechanism is not activated, trap-jaw ants use their mandibles as slow, multi-degrees of freedom manipulators when actuating them directly with muscle contractions (Fig. 1B). To our knowledge, the joint configuration and constraints of a spring-loaded head have yet to be studied.

To solve how spring propulsion energetics, rotational dynamics and joint mechanics enable tiny joints and ultrafast angular velocities, we tested live animals and modeled the LaMSA system found in *Odontomachus* trap-jaw ants by integrating experimental kinematics, morphology, geometry of energy delivery and rotational dynamic modeling of joint and energy delivery configurations. We addressed the following questions. (1) Based on the morphology and kinematics of live animals, how is elastic energy storage and recoil configured in the trap-jaw ant's head? (2) Given the geometry of live animals and the energy required to accelerate the mandibles, how is elastic potential energy transformed into torque on the mandibles? (3) Based on a generalizable, dynamic mathematical model that is equivalently sized to trap-jaw ants, which joint and spring configurations enable ultra-rapid rotation given the proportion, amount and location of elastic energy delivered to tiny, rotating beams? This study provides an experimental and modeling framework for fast, tiny rotations driven by torquegenerating spring-based propulsion. These ultrafast, spring driven, repeated-use rotations at small scales are common in biological LaMSA and have not yet been achieved in synthetic systems.

MATERIALS AND METHODS

Study species, animal collection and maintenance

An *Odontomachus brunneus* (Patton 1894) (Formicidae: Ponerinae) colony was collected with permission from the Archbold Field Station, FL, USA, and kept in the lab at room temperature (24–27°C) (Permit number P526P-16-00459). We provided the colony with a constant supply of water and sugar water. Two to three crickets were also given to the colony per week to provide dietary protein.

Morphological measurements and 3D reconstruction

We measured mandible, head and body dimensions of the trap-jaw ants. First, we measured body mass, then detached the head from the body and measured head mass. We photographed the ant using a dissection microscope (M165FC, Leica, Buffalo Grove, IL, USA). We then split the head in half along the midline, isolated the mandibles and removed all tissues within the head capsule (mandibular muscles, muscles controlling the other mouth parts and the antennae, connective tissue and nervous system). We weighed each mandible and the head capsule. All masses were measured to the nearest 0.01 µg with a microbalance (XPE56, Mettler Toledo, Columbus, OH, USA). Body lengths were measured to the nearest 0.1 mm and mandible lengths to the nearest 0.01 mm (M165FC, Leica; stage micrometer, KR-814, Microscope World, Carlsbad, CA, USA). We collected an additional dataset of mandible in- and out-lever lengths and adductor apodeme lengths based on 9 individuals (18 mandibles total). Based on prior morphological research of head/joint configuration for muscle-driven mandible movements, we defined in-lever as the distance from the apodeme attachment to the hypothesized external joint articulation (Gronenberg, 1995a,b). The out-lever is the distance from this

hypothesized joint articulation to the distal tip of the mandible. We tested the energetic consequences of this assumption of the lever ratio via mathematical modeling (see below).

We calculated the mandible muscle mass for each mandible by subtracting mandible mass and head capsule mass from the total head mass and dividing by two. The mandible adductor constitutes approximately 70% of the muscle mass in the head with 10–20 times greater volume than the remaining mandible muscles (Gronenberg, 1995a,b). Therefore, we used the total mandible muscle mass per mandible to calculate a conservative estimate of muscle power amplification and energy density (i.e. we over-estimated the mass of the muscle used for closing the mandibles). We calculated power amplification using the classic mathematical inference for the presence of spring propulsion (mechanical power output of the mandible rotation divided by the mass of the adductor muscle) (Longo et al., 2019). Even though it would have been ideal to measure only the mandible adductor mass, we were unable to avoid the rapid dehydration that accompanied a lengthier dissection of each muscle or the opposite issue of excessive water mass from a submerged preparation; therefore, we chose instead to simply underestimate power amplification by overestimating adductor mass through the above method. If the measured power/mass ratio was larger than the maximum observed from striated muscle (approximately 300 W kg⁻¹; Askew and Marsh, 2002), we would conclude that this motion is primarily actuated by elastic recoil of head structures instead of muscle (Longo et al., 2019). Data are presented \pm s.d., with analysis performed in Mathematica 12.0 and Microsoft Excel.

Micro-computed tomography (μ CT) images were acquired by scanning an ethanol-dehydrated ant head in a relaxed (not springloaded) configuration. Because the spring-loaded configuration is a transient behavior, it is not reflected in preserved trap-jaw ants. To enhance contrast, the head was sputter-coated with gold nanoparticles prior to scanning (XTH 225 ST, Nikon Metrology Inc., Brighton, MI, USA). Digital image processing to generate images was performed using 3D Slicer (Fedorov et al., 2012) and Fusion 360 (Autodesk, San Rafael, CA, USA).

High speed imaging

To measure head deformation and assess its role in elastic energy storage and delivery, we filmed 10 videos (10 individuals, 1 video per individual) of the head flexion during loading. A stage micrometer (KR-814, Microscope World) was used to calibrate the length scale of the videos, such that our measurement accuracy, limited by the resolution of our stage micrometer, was 20 µm. However, our pixel resolution was far greater and extended to 3.2 µm, thus allowing more precise measurements within the experimental setup, but with the caveat that our accuracy extends only to 20 µm given the limits of the stage micrometer. Each ant was mounted via a pin that was attached to the dorsal surface of the head with a piece of dental wax such that the camera could have an unobstructed ventral view of the head and the mandibles during filming. The strikes were triggered by applying slight air pressure to the anterior side of the ant head. Prior to filming, we aligned the ant's head such that the plane in which the two mandibles rotated was perpendicular to the filming direction.

To calculate strike kinematics, we collected high speed image sequences of strikes in 10 *O. brunneus* workers with five strikes per worker, yielding a total of 99 individual mandible movements (one mandible movement was out of focus and unusable) (256×128 pixels, 2.33 µs shutter duration, 300,000 frames s⁻¹, Photron SA-Z, Photron, San Diego, CA, USA) with a mounted lens (Nikon 105 mm AF Micro-Nikkor, Nikon, Tokyo, Japan).

Kinematics

We tracked the position of the mandible tips and calculated the angular rotation of both mandibles during strikes. The image sequences were digitized by manual tracking (v.10, Fiji) (Schindelin et al., 2012) to extract the cartesian coordinates of each mandible tip (x_i, y_i) . We stopped tracking the tip when it was no longer visible, which was usually caused by the interaction between the two mandibles. The center of rotation (x_c, y_c) was found by a circular regression which minimized the sum of squared radial deviations. This approach identified the center of rotation mathematically to allow us to remain agnostic about the morphological location of the center of the mandible's rotation. The rotation angle θ was defined as the angle between $\overrightarrow{r_i}$ and $\overrightarrow{r_1}$, where $\overrightarrow{r_i} = (x_i, y_i) - (x_c, y_c)$, $i = 1, 2, 3 \dots$ The reference line for calculating θ was set as the static (opened laterally) position of the mandible before the strike. Consequently, rotation of both the left and right mandibles could be described by θ . We analyzed the data using custom programs (v.8.6, MATLAB, The MathWorks, Inc., Natick, MA, USA).

For each strike, we reduced the noise in the raw angular displacement data using the *smooth* function in MATLAB, with a span of five points for the moving average. This approach reports the mandible angle at any given time t as the average angle measured for five frames (two frames prior to t, the frame at t, and the two frames after t). We calculated raw angular velocity between two consecutive frames as the difference in smoothed angular displacement divided by the time interval (1/300,000 s). We then applied the same smoothing procedure to raw angular velocity, which we used for all subsequent kinematic and energetic calculations. We report angular acceleration as maximum angular speed divided by the time from the beginning to the time at which maximum speed is reached. This time-averaged angular acceleration may underestimate the real peak acceleration.

Kinematic, energetic and power amplification calculations

Strike linear velocity and acceleration were calculated as the product of angular velocity and the length of the mandible out-lever, which was 90% of the total mandible length (see out-lever measurements in 'Morphological measurements and 3D reconstruction', above, and tests of this assumption in 'Dynamic modeling of spring actuation mechanics', below). We calculated maximum rotational kinetic energy (KE_{max}) as $\frac{1}{2}I\omega_{max}^2$, where I is the mass moment of inertia of the rotating mandible and ω_{max} is the maximum angular velocity during a mandible movement. Simplifying the mandible as a homogeneous rod rotating around a pivot with the pivot located 10% of the mandible length from the proximal end (based on the morphology measurements above), we calculated I as $(1/12)mL^2+m(0.4L)^2$, where m is the mandible mass and L is the mandible length. Maximum mechanical power (P_{max}) was then calculated as KE_{max} divided by the time to reach 90 deg (the point at which the tip of the mandible is in its most anterior position). As is the case for the calculation of acceleration, this is a time-averaged value and underestimates the instantaneous power. Finally, we calculated energy density and power density of the system by dividing KE_{max} and P_{max} by the mandible adductor mass. Data are presented as means±s.d.

We determined the transition between powered mandible rotation (mandibles accelerated by spring recoil) and unpowered mandible rotation (mandibles decelerate after recoil ends) based on the timing and angular rotation of the mandibles when they transition from accelerated movement to deceleration. We calculated the angle of the mandibles at which this transition occurred and the energy required to accelerate the mandibles to this position, and then

determined the amount of displacement required at the base of the mandibles to generate this rotation.

Given that mandible rotation occurs in a single plane (see above), the displacement of the base of the mandible that is relevant to powered rotation is also in that same plane. This observation allows a substantial simplifying assumption about energy delivery to the mandibles: even though head capsule deformation is a threedimensional process, the only aspect of this deformation that is relevant to generating powered rotation occurs in the plane of the mandible's displacement. Therefore, we can ignore the complex elastic deformations of the whole head, which are important for the mechanism of elastic energy storage of the system but are irrelevant to the elastic recoil displacement that causes mandible rotation. In other words, the total elastic energy stored in the head capsule requires 3D head deformation, but multi-axis head deformation is (and must be) transformed to planar elastic energy delivery to rotate the mandibles. This simple observation is crucial for distinguishing between the mechanism of elastic energy storage and the mechanism for transforming elastic potential energy to torque – we are doing the latter here.

We calculated the propulsion energy accounted for by the measured lateral and anterior displacement of the head capsule in the mandible's plane of motion (see 'High speed imaging' above). The difference between the energy calculation based on the spring-powered part of the mandible strike and the energy calculation based on lateral and anterior head capsule displacement is approximately the amount of spring-based energy powering the mandibles by the muscle–apodeme unit. Muscle–apodeme recoil is internal – it is not visible via head deformation. As addressed in the Results, the internal muscle–apodeme recoil is crucial for energy accounting and the overall mechanism for elastic energy delivery and torque generation on the mandibles.

See datasets and Mathematica code (Dryad, https://doi.org/10. 5061/dryad.c2fqz61bs) for these geometric calculations of beam displacement and rotation.

Dynamic modeling of spring actuation mechanics

Given the results of the above analyses, we hypothesized a mechanism by which spring-based propulsion develops torque on trap-jaw ant mandibles. Based on these findings, which are detailed in the Results, we developed a dynamic model that incorporates the dynamics of the force couple-like behavior of two springs actuating a beam at two locations to yield rotation. We tested how the energetic proportion and positioning of dual springs influence the need for a constrained pin joint and affect the mechanical power output of the system (Fig. 2).

Given the limitations of high speed video resolution at this small temporal and spatial scale, precise localization of the application of force from head recoil to the mandible was not possible; therefore, to improve the accuracy and check the viability of our dynamic model, we tested and simulated multiple configurations of elastic energy delivery and joint constraints using the dynamics and dimensions of the mandible strike. First, we tested the effects of lever arm proportions on the calculated strike energetics, given that our original energetic calculations in live trap-jaw ants were based on a pivot point location at 10% of the lever arm. This is the location of the pivot for muscle-driven (not spring-driven) movement based on prior anatomical work. Second, to address whether spring energy delivery can be configured to reduce the need for joint constraints and associated dissipation, we tested alternative models for joint constraints. In one model, the mandible was constrained to move in a circular arc (as if there were a mechanical 'pin' joint fixed to the

mandible). In a second model, the mandible was kinematically unconstrained, such that spring recoil of the head and apodeme was allowed to produce arbitrary motion of the mandible. We did not model the pin joint to have any dissipation, such that the model would provide a conservative assessment of the power comparisons of these two cases (i.e. not energetically penalizing pin joints over unconstrained joints).

A two degrees of freedom dynamic model of the ant mandible was constructed by approximating the mandible as a thin, uniform rigid bar driven by two recoiling springs. The two degrees of freedom are translational movement as the mandible moves anteriorly and rotational movement of the mandible. The two springs represent the muscle—apodeme unit, loaded in tension, and the head capsule, loaded in compression. The equations of motion for the mandible are derived with respect to a coordinate system placed equidistant between the two springs. In the dynamic model, we assume that the forces from the springs only act along the *y*-direction and given these constraints to the system, there is no lateral acceleration in *x* as there are no lateral forces applied to the system. Additionally, a gravity term is not included as the mandible moves in a plane orthogonal to gravity. The equations of motion for the mandible are as follows:

$$m\frac{\mathrm{d}^{2}y}{\mathrm{d}t^{2}} = k_{\mathrm{hc}} \left(y_{\mathrm{hc0}} - y - \frac{L_{\mathrm{total}} - L_{\mathrm{hc}}}{2} \sin(\theta) \right)$$
$$- k_{\mathrm{mau}} \left(y_{\mathrm{mau0}} + y - \frac{L_{\mathrm{total}} - L_{\mathrm{hc}}}{2} \sin(\theta) \right), \qquad (1)$$
$$+ mL_{\mathrm{cm}} \left(\frac{d\theta}{\mathrm{d}t} \right)^{2} \sin(\theta)$$

$$\begin{split} I_{\rm p} \frac{\mathrm{d}^2 \theta}{\mathrm{d}t^2} = & \left(\frac{L_{\rm total} - L_{\rm hc}}{2} \right) \cos(\theta) \left(k_{\rm hc} \left(y_{\rm hc0} - y - \frac{L_{\rm total} - L_{\rm hc}}{2} \sin(\theta) \right) \right. \\ & \left. + k_{\rm mau} \left(y_{\rm mau0} + y - \frac{L_{\rm total} - L_{\rm hc}}{2} \sin(\theta) \right) \right) \,, \end{split}$$

where $k_{\rm mau}$ is the tensile spring constant of the muscle–apodeme unit; $k_{\rm hc}$ is the compressive spring constant of the head capsule; and $y_{\rm mau0}$ and $y_{\rm hc0}$ are the initial displacements of the respective springs, related to the loading before striking. $L_{\rm total}$ is the distance from the mandible tip to the tensile spring attachment point, and in this model, the spring attachment point is always at the end of the mandible, resulting in $L_{\rm total}$ being equal to the full length of the mandible (L), and $L_{\rm hc}$ is the distance from the mandible tip to the compression spring attachment point. m is the mass of the mandible and $I_{\rm p}$ is the mass moment of inertia of the mandible rotating about a point halfway between the attachment points of the two springs. The full derivation and MATLAB code are available from Dryad (https://doi.org/10.5061/dryad.c2fqz61bs). The mass moment of inertia at this point is calculated using the parallel axis theorem and is given generally as:

$$I_{\rm p} = I + m(L_{\rm hc} - \frac{L_{\rm total}}{2} + \frac{L_{\rm total} - L_{\rm hc}}{2})^2,$$
 (3)

where I is the mass moment of inertia of a uniform slender rod at the center $(I=1/12mL_{\rm total}^2)$ and $L_{\rm total}$ is the total length of the mandible. Moving the attachment of the head capsule spring along the mandible through the ratio of the distance from the tip of the mandible to the head capsule and the total mandible length $(L_{\rm hc}/L_{\rm total})$ changes the mass-moment of inertia.

The simulation starts with the mandible at rest at 0 deg with no initial angular or translational velocity and any effect of unlatching is not modeled here. The initial displacement of the springs ($y_{\text{mau}0}$) and y_{hc0}) and head capsule stiffness (k_{hc}) were all calculated relative to a fixed spring constant for the muscle-apodeme spring (k_{mau}) of 3000 N m⁻¹ and energy ratio in the muscle–apodeme spring (E_{mau}) E_{total}) relative to the whole system of 24.2 μ J from the measured kinematics. We calculated 3000 N m⁻¹ as follows: (1) 65 deg mandible rotation requires that the head and muscle-apodeme unit displace the mandible by 127 µm; (2) the system must have at least 24.2 μ J; (3) energy is equal to $1/2kx^2$; (4) these three calculations can be solved for k, yielding an estimate of 3000 N m⁻¹ stiffness. The result approximates the complex deformation of the head capsule as a single spring element, as explained in the previous section. The energy partitions were swept in the maps from 1% to 99% in 1% increments, going from a system with almost all the total system energy in the head capsule (1%) to one with almost all the total system energy to the muscle apodeme unit (99%). Sweeping these energy partition values changes the initial deformation of the springs, and stiffness of the head capsule spring, but the model does not explicitly limit these parameters to biologically relevant values, allowing us to explore a large parameter set within these maps. The whole system energy was measured from the system's kinematics, and the spring constant was estimated so that measured deformation of the elastic elements resulted in the observed kinetic energy (i.e. the two springs always have a total energy of 24.2 μJ). Integrating the dynamics using a forward Euler method allowed for the force in the tensile spring to be monitored during closing. The spring representing the muscle-apodeme unit can only act in tension in vivo; therefore, the numerical integration technique set the force in the muscle–apodeme spring to zero when the mandible moved to a position that would result in a compressive action of the spring. The rotational and linear displacements of the mandible were solved until the mandible reached 65 deg of rotation, the angle at which the mandible is no longer powered by the elastic elements. Power is calculated in the simulation by:

$$P = \frac{1}{2} I_{\rm p} \omega_{\rm max}^2 / t, \tag{4}$$

where ${}^{1}\!\!/\! I_p\omega_{\rm max}^2$ is the rotational kinetic energy of the mandible at 65 deg and t is the duration required to reach 90 deg, with the assumption that momentum closes the mandible from 65 deg to 90 deg.

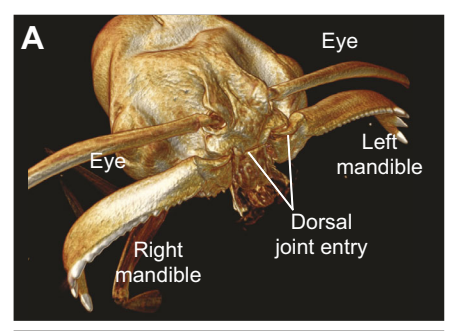
The sensitivity of power with respect to initial energy and lever arm ratio was simulated only for the two degrees of freedom model with the proportion of energy evenly split between the head capsule and muscle–apodeme equivalents in the model. The initial energy was simulated from 18.15 μJ to 30.25 μJ in 0.242 μJ increments. This range encompasses 1 s.d. of the calculated energy from the experimental kinematic data. The lever ratio ($L_{\rm hc}/L_{\rm total}$) was varied from 80% to 99% in 1% increments. The dynamics were simulated for each combination of initial energy and lever ratio, and the resultant power was calculated as described previously.

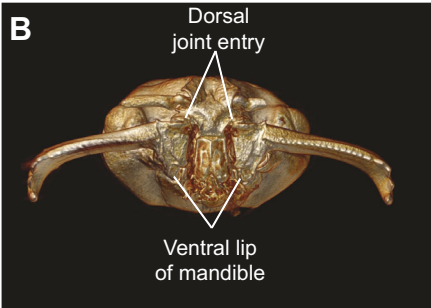
All simulations were solved numerically using a forward Euler method with a timestep of 1 ns using MATLAB (MATLAB 2018a, The MathWorks, Inc.). Animations of the simulated mandible closing for select points are shown in Movie 2.

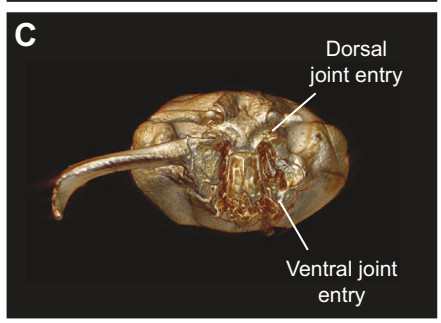
RESULTS

Morphological measurements and 3D reconstruction

We visualized head morphology, measured head deformation, and experimentally quantified the head's role role in elastic energy storage and mandible actuation (10 individuals, 1 video per individual) (Figs 3 and 4). Prior to the strike, muscle contractions deformed the head both antero-posteriorly and medio-laterally in







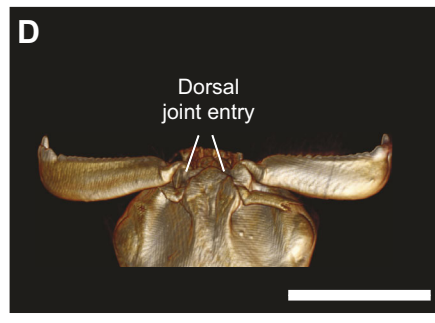


Fig. 3. Trap-jaw ant mandibles attach externally to the head via a relatively unconstrained joint. (A) Odontomachus brunneus workers strike with large mandibles that attach via an unusual joint morphology to the anterior region of the head that permits multi-degrees of freedom movements when actuated directly by muscle during slow manipulative movements (Fig. 1B). (B,C) In these anterior views of the mandible external attachment sites with both mandibles attached (B) and with the left mandible removed (C), the mandible is positioned externally to the head. Note that these images are in the configuration of the head for muscle- (not spring-) driven movement. The ventral lip is loosely attached externally and can be slid internally or externally as part of a latch mechanism. Odontomachus mandible joint morphology is extensively detailed in previous research (Gronenberg, 1995a,b). (D) This dorsal view shows the proximal region of the mandible that slides externally when the mandibles are open. This anterior surface of the head is only in contact with the externally visible base of the mandibles during initial rotation and head recoil (see Fig. 5). Scale bar: 1 mm.

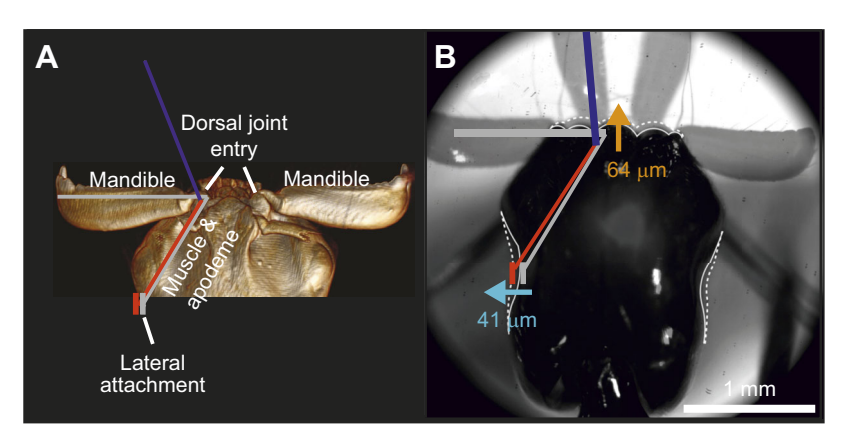


Fig. 4. Rotation of the mandibles occurs in the same plane as the elastic recoil of visualized head deformation. (A) An overlay on the dorsal view of the ant head (anterior toward top of page) illustrates how the adductor muscle–apodeme unit connects at the medial lip of the left mandible. The lateral attachment simplifies the three-dimensionality of the internal muscle attachments to indicate the location of lateral displacement of head recoil. The gray lines indicate the position when the mandibles are open. When in closing positions, the components are indicated in color (mandible: purple; muscle–apodeme: red). (B) Two frames of a high speed video are overlaid to show head deformation during the loaded configuration (solid white lines) and after the mandibles are fired (dashed white lines). As the mandibles close, the head bows out laterally by 41 μm and recoils anteriorly by 64 μm in the plane of motion of the mandibles. The overlaid kinematic model represents the resultant planar head deformation relevant to actuation of mandible rotation in that plane.

the plane of mandible rotation. The antero-posterior deformation averaged $64\pm14~\mu m$ (3.2% reduction in length) and each side bowed in medially by $41\pm9~\mu m$ (6.0% decrease in width of head) (Figs 3 and 4). This deformation substantially changed the shape of the head (Fig. 4): it shortened antero-posteriorly while the sides bowed inward toward the midline.

To calculate the relative roles of propulsion by head deformation and the stretching/contracting muscle–apodeme unit, we measured mandible strike kinematics, mandible dimensions and mass (Figs 5 and 6, Table 1). Trap-jaw ant body mass was on average 5.97 ± 0.98 mg, with an antero-posterior body length of 7.59 ± 0.46 mm (N=10 ants for all measurements). Individual mandibles averaged 1.38 ± 0.06 mm length along the distal–proximal axis, with an average mass of 54.5 ± 9.1 µg (individual left/right mandible measurements are presented in Table 1). The mandible adductors together constituted 14% of the body mass of the entire animal (0.81 ± 0.13 mg). The moment arm of the mandibles averaged 10% of the length of the entire mandible ($10.0\pm1.3\%$). The average length of the head capsule was 1.98 ± 0.14 mm, and the length of the distal part of the adductor apodeme averaged 294 ± 22 µm.

Kinematics, energetics and power amplification

During a mandible strike, the mandibles rotated from their initial position (locked laterally, 0 deg of rotation) to a position pointing anteriorly (rotated 90 deg) with an average duration of $77.1\pm7.4~\mu s$ (range $65-106~\mu s$; s.d. <10% of the mean) (Figs 4-6). The mandibles rotated with a maximum angular velocity of $44,200\pm4500~rad~s^{-1}$, with the tips of the mandibles reaching a linear speed of $54.4\pm5.6~m~s^{-1}$. The mandibles reached their maximum velocity when rotated $65.2\pm1.0~deg$ (Fig. 6), after which they decelerated. Therefore, after the initial 65~deg of rotation, the mandibles are most likely unpowered (i.e. no longer spring actuated).

Based on this transition from the mandible rotation powered by recoil (65 deg) and not powered by recoil (65–180 deg and subsequent oscillations), we calculated mandible kinetic energy during the range of motion when elastic energy stored in the head and muscle–apodeme unit is transformed into kinetic energy of mandible rotation (the first 65 deg of mandible rotation). Therefore, our calculation of kinetic energy includes only the spring actuation phase and assumes that energy calculated only during the first

65 deg of rotation provides a conservative estimate of the elastic energy recoil delivered to the mandibles. With this assumption, the motion of one mandible required an average of 24.2 \pm 6.0 μ J of elastic potential energy and 0.32 \pm 0.09 W of power. The ratio of average power output and the mass of the adductor muscles was 396,000 W kg⁻¹.

Given the deformation required to rotate the mandibles for the first 65 deg of rotation (Fig. 6, powered rotation prior to deceleration), we found that head deformation in the plane of the mandible rotation (64 µm of anterior displacement and 41 µm of lateral displacement) accounted for 33 deg of powered mandible rotation. The remaining spring-actuated mandible rotation can be explained by internal recoil of the muscle–apodeme unit. The muscle–apodeme unit accounts for the remaining deformation of the powered rotation by straining no more than 4.4% (Fig. 4), which is consistent with properties and maximum strain of biological elastic muscle–tendon mechanisms (Bennet-Clark, 1975; Lieber et al., 1991; Moo et al., 2017). Therefore, the deformation required for spring-powered mandible rotation is fully accounted for based on head recoil and muscle–apodeme unit recoil.

Spring actuation mechanism: dual spring force couple

Given the findings that a combination of head recoil and muscleapodeme recoil is sufficient to power the mandibles during their spring-actuated acceleration, we hypothesize a generalized twospring mechanism for developing torque in this system (Fig. 2). Based on head and adductor muscle morphology (Gronenberg, 1995a,b), head deformation during elastic recoil and the transition from spring-actuated to unpowered rotation of the mandible, we propose that the trap-jaw ant's elastic mechanism operates as two springs operating in series and delivering energy at two locations along the mandible to develop a torque. We term this mechanism a 'dual spring force couple'. In this configuration, the head capsule and muscle-apodeme unit both store elastic energy, they apply forces in opposite directions, and thus develop torque along the mandible as the elastic energy is released. As the two springs recoil, the recoil of the muscle-apodeme unit pulls the mandible, while the head capsule deformation pushes the mandible.

For the sake of thoroughness, we tested alternative single spring models. To achieve the observed energetics and stable center of

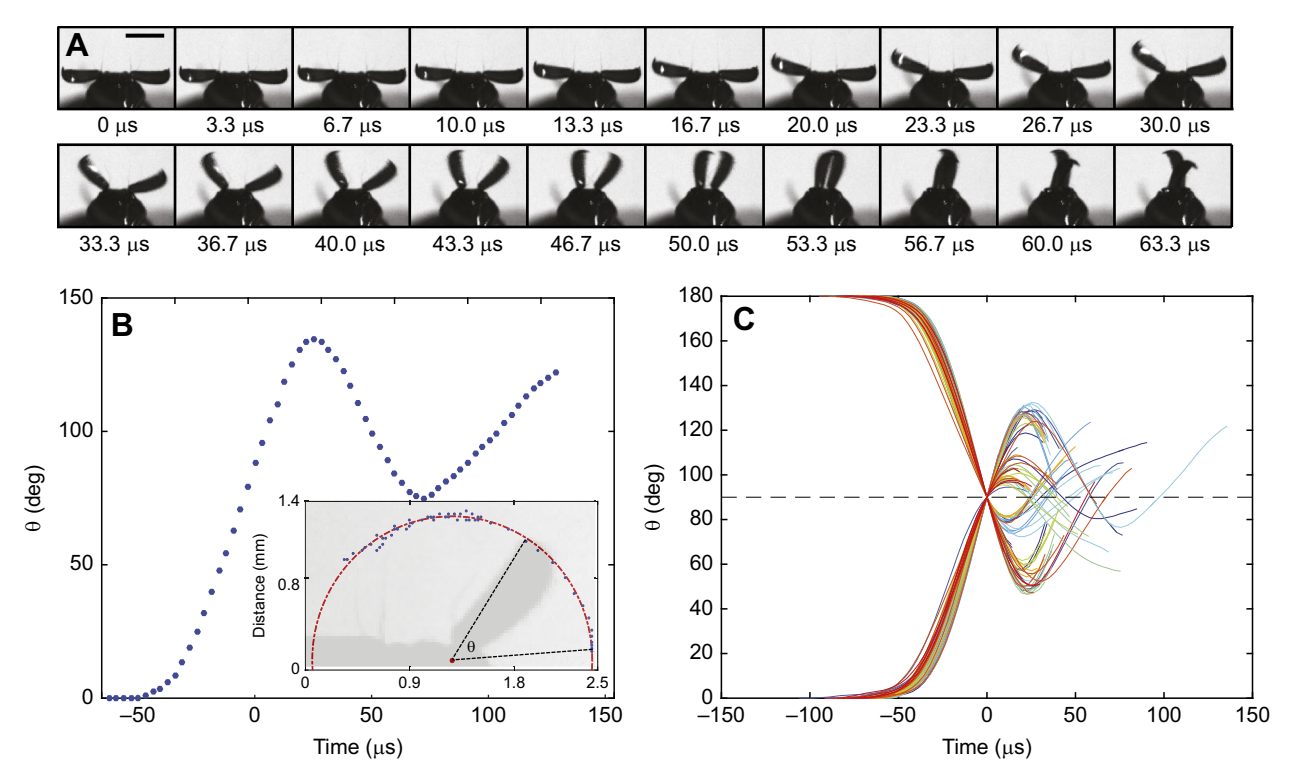


Fig. 5. Trap-jaw ant mandibles rotate rapidly through a precise circular arc that transitions to unconstrained motion after crossing the midline. (A) *Odontomachus brunneus* rapidly close their jaws within an average of 77 μs (Table 1). The mandibles rotate medially; in this sequence, one mandible rotates slightly out of plane later in the strike, which occurred after spring-based propulsion was completed. Strikes were filmed from a ventral view (anterior toward the top of the page). The image sequence progresses from left to right, top row to bottom row. The time interval between consecutive frames is 3.333 μs. Scale bar: 1 mm. (B) Mandible rotation circumscribes a nearly circular motion (inset: distal tip of mandible tracked at 3.3 μs intervals) during spring actuation. (C) Mandible rotation exhibits minimal variation prior to crossing the midline (time=0) when actuated by spring recoil. Mandible strikes are plotted with each color representing an individual ant (10 individuals; 5 strikes per individual; 99 individual mandible movements; one mandible movement was out of plane, and thus was not usable for data analysis). To align the traces, we set the left mandible strikes to start from 0 deg, and the right mandible strikes to start from 180 deg. We set *t*=0 as the moment when a mandible first passes 90 deg (the midline). The symmetry with respect to 90 deg (black dashed line) indicates minimal difference in the angular trajectories between the left and right mandibles. Because of the time alignment performed on the data, the delay in the onset between the left and right mandible strikes is not visible.

rotation using a single recoiling spring attached to the proximal end of the mandible would require a zero stiffness head capsule with twice the displacement of the muscle-apodeme unit to achieve the same spring deformation as a dual spring. However, doubling the length change of the apodeme is not possible, given the size limitations of the trap-jaw ant head. Alternatively, if the only spring is the head capsule, then, given the geometry of mandible rotation and the measured head displacements along the plane of the mandibles, the mandibles could only be accelerated by spring recoil to 30 deg rotation, which does not match our kinematic data showing deceleration starting at 65 deg. Finally, as established by the extremely high power density of the strikes, and the limits on muscle contraction duration and power, none of the ultrafast rotation can be powered by an active muscle contraction: these are exclusively spring-actuated movements.

Dynamic modeling of spring actuation mechanics

Using this generalized dual spring force couple, we then performed simulations to test how energy is delivered through the dual spring force couple to yield rotation of the modeled mandible across varying joint constraints. We further tested how the energetic proportion and positioning of dual springs affect the output motion, ultimately influencing the need for a constrained pin joint and affecting the mechanical power output of the system (Fig. 7).

The respective placement of the springs affected the power output of the system. We simulated each spring attaching to a different place along the mandible with the springs' propulsion causing reaction forces at the center of rotation. These reaction forces are a function of the location of each spring's contact with the mandible and the amount of energy stored in each spring. Head recoil applies force directly at the attachment, which we varied across models, while muscle—apodeme unit recoil applies force at the end of the mandible's moment arm. Therefore, the relationship between each spring's recoil, the resulting mandible rotation and the reaction force at the center of rotation differ depending on whether a larger percentage of energy is applied by the head recoil (which applies force at the attachment) or whether a larger percentage is applied by muscle—apodeme recoil (which applies force at the proximal end of the mandible's moment arm).

Separating the springs by a greater distance causes the springs to have a greater mechanical advantage, apply a greater torque to the mandible and increase power output. This separation also decreases the angular displacement over which the force is applied – again increasing power. Storing a larger fraction of energy in the tensile spring ($E_{\text{mau}}/E_{\text{total}} \rightarrow 1$) (the muscle–apodeme unit) generally produces a larger moment on the mandible than the head deformation recoil, allowing the 24.2 μ J of energy to be transferred more quickly from the spring to the mandible. To maximize power output, these two effects should be combined, which results in 100% of the energy being stored in the muscle–apodeme unit, with as large a distance as possible

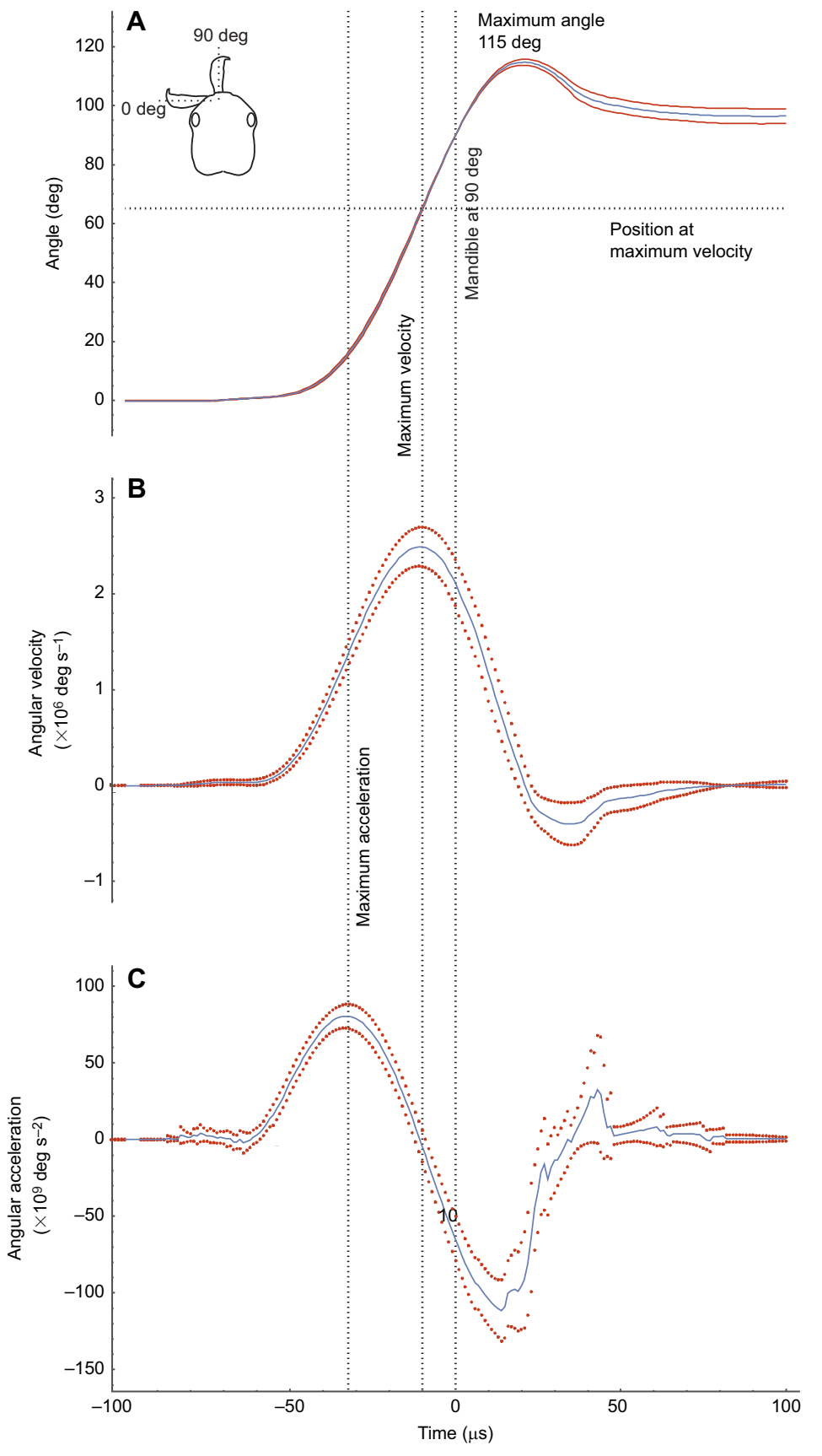


Fig. 6. Minimal variation of strike kinematics results in consistent profiles of angle, angular velocity and angular acceleration, and reveals that elastic recoil powers only the first 65 deg of mandible strikes. Average (blue) and 1 s.d. (red) of the angle (A), angular velocity (B) and angular acceleration (C) of 99 mandible movements from 10 ants. Strikes are aligned at time zero which is defined as 90 deg mandible rotation. A mean for each ant's kinematics was calculated across its 10 mandible movements (five strikes, two mandibles per strike), and then the 10 individual means were averaged to produce the plots above. Vertical dotted lines indicate the time of maximum angular acceleration and angular velocity, and when the mandible reaches its anterior-most position (an angle of 90 deg). The mandible reaches its maximum velocity at 65 deg of rotation (A,B), showing that elastic recoil only drives the first 65 deg of a mandible strike.

Table 1. Morphology, jaw-closing kinematics and energetics

	_	
Measurement		Means±s.d
Body length (mm)		7.59±0.46
Body mass (mg)		5.67±0.98
Mandible length (mm)	Left	1.37±0.06
	Right	1.4±0.07
Mandible mass (μg)	Left	54.7±10
	Right	53.3±8.2
Mandible adductor mass (mg)		0.81±0.13
Strike duration (µs)		77.1±7.4
Delay between mandibles (µs)		2.47±2.08
Maximum angular velocity (10 ⁴ rad s ⁻¹)		4.42±0.45
Maximum linear velocity (m s ⁻¹)		54.4±5.6
Angular acceleration (108 rad s ⁻²)		7.12±1.17
Kinetic energy (µJ)		24.2±6.0
Power (W)		0.32±0.09

Data are shown for 10 strikes each by 10 *Odontomachus brunneus* workers (99 mandible movements; one mandible movement was out of plane).

between the apodeme and pivot. Note that this is the opposite of what would be predicted to maximize velocity output under static conditions (i.e. configure the smallest moment arm).

However, this configuration (100% energy stored in the muscleapodeme unit) can only generate the observed circular trajectory of mandible motion if the mandible has large reaction forces at a 'pin' joint that constrains mandible rotation and if the muscle-apodeme unit lengthens by up to 8.8%, which is unlikely based on maximum strain in other biological systems (Snedeker and Foolen, 2017). In contrast, an equal distribution of energy across both springs achieves 38% less power than storing 100% of the energy in the muscle–apodeme unit. This yields a power output of 0.35 W, which is within 1 s.d. of the power output observed in vivo (0.32±0.09 W). Further, a distribution of energy across both springs results in no difference in the motion of the mandible between a pin-constrained mandible and a mandible lacking joint constraints (Fig. 7); both systems exhibit pure rotation, and no translation. Therefore, the power delivered by these systems is equal. Thus, purely circular motion can be ascribed to the distribution and recoil of the springs without a kinematic constraint like a pin joint. An equal energy distribution of the springs is required for a stationary instant center of rotation without a kinematic constraint.

The calculated mandible kinetic energy based on the hypothetical 10% location of the pivot (see Materials and Methods) did not affect these findings (Figs 7 and Figs 8). The simulations varying the initial energy and lever ratio express the sensitivity of power with respect to the uncertainty of the measured lever ratio and calculated energy from the kinematic data. An uncertainty of 1% on the lever ratio with a 24.2 µJ initial energy exhibits a range of output power from 0.32 to 0.38 W, which is well within the standard deviation of the calculated output power from the kinematic data. An uncertainty of 6 µJ for the initial energy with a 90% lever ratio simulation exhibits a power output of 0.26–0.44 W, slightly outside of 1 s.d. of the calculated power of 0.32±0.09 W, although with a similar range. Overall, the uncertainty of the dynamic model reflects the uncertainty within the measured and calculated experimental data. The map of the sensitivity shows similar trends to those described above, where power output increases with decreasing lever ratios (Fig. 8). Naturally, power output also increases with increased initial energy and even reaches a maximum of 0.66 W for an 80% lever ratio and initial energy of 30.3 µJ.

DISCUSSION

Through our integrative approach of visualizing trap-jaw ant head deformation and mandible rotation and using these empirical

results to inform mathematical modeling, we answered the guiding questions of this study. We found that trap-jaw ants store elastic energy in their head capsule and muscle-apodeme units to form a dual spring force couple mechanism. The elastic potential energy is transformed to kinetic energy through the simultaneous recoil of the head and muscle-apodeme unit to generate ultrafast rotational torque on the mandibles. Dynamic modeling at the scale of spring-powered trap-jaw ant mandible strikes reveals that a dual spring force couple substantially reduces – and possibly eliminates - the need for joint constraints to achieve precise and rapid rotations at small scales. A general mechanism of a dual spring force couple is consistent with the morphology and mechanisms of multiple other ultrafast, rotating LaMSA mechanisms in biology and provides new design insights for small engineered systems, such as micro-electromechanical systems (MEMS) and micro-robots.

Energy delivery via dual spring force couples

Trap-jaw ants store and deliver elastic energy using a dual spring force couple mechanism achieved through deformation of their head capsule and muscle–apodeme units. Their two distinct morphological springs operate in tandem as energy is delivered in two places to develop torque along the mandible. We define this new term and mechanism – dual spring force couple – as occurring when two springs recoil simultaneously to deliver energy to two different locations. Rotation-generating force delivery operates as a force couple through direct spring actuation.

A conservative estimate of the muscle mass-specific power of their mandible strike is 396,000 W kg⁻¹, which further establishes the use of elastic recoil to power this movement. Muscle actuation has a maximum mass-specific power output (100–400 W kg⁻¹), which is far below the trap-jaw ant strike's remarkable power density (Alexander and Bennet-Clark, 1977; Askew and Marsh, 2001; Longo et al., 2019).

The kinematic analyses of the ultrafast strikes revealed a stationary center of rotation of each mandible and precise circular arc as it rotates through the 77 µs of closure (Figs 5 and 6). The limited depth of field of the high speed imaging system (less than 100 µm) caused out-of-plane movement to be out of focus; even so, until crossing the midline, the mandibles exclusively rotated in focus and, therefore, within a planar arc (Fig. 5). The rotational movements were so precise before crossing the midline that they permitted calculation of second derivative accelerations (which are normally prone to error amplification), which indicated that the mandibles accelerate only during the first 65±1.0 deg of rotation toward the midline (Fig. 6). Once the mandibles pass the midline, the movement of each mandible's tip is no longer circular and lacks a fixed point of rotation (Figs 5 and 6). This combination of precise motion during spring actuation followed by minimally constrained motion later in the movement highlights the inherent multiple degrees of freedom of the mandible joints. A similar range of movement is exhibited when the mandibles are actuated directly with muscle (i.e. when not using the LaMSA mechanism) (Fig. 1B) (Gronenberg, 1995a,b).

Dual spring force couples may be a general principle for arthropod LaMSA systems, in which a combination of exoskeletal springs and elastic apodemes is used for generating torque through elastic recoil while minimizing wear and stress on the joints (Fig. 2). For example, spearing mantis shrimp likely use a dual spring force couple of the exoskeleton and extensor apodeme (Rosario, 2015), although this has not been identified as such. Grasshopper legs exhibit a 55%:45% energetic split between the semi-lunar process

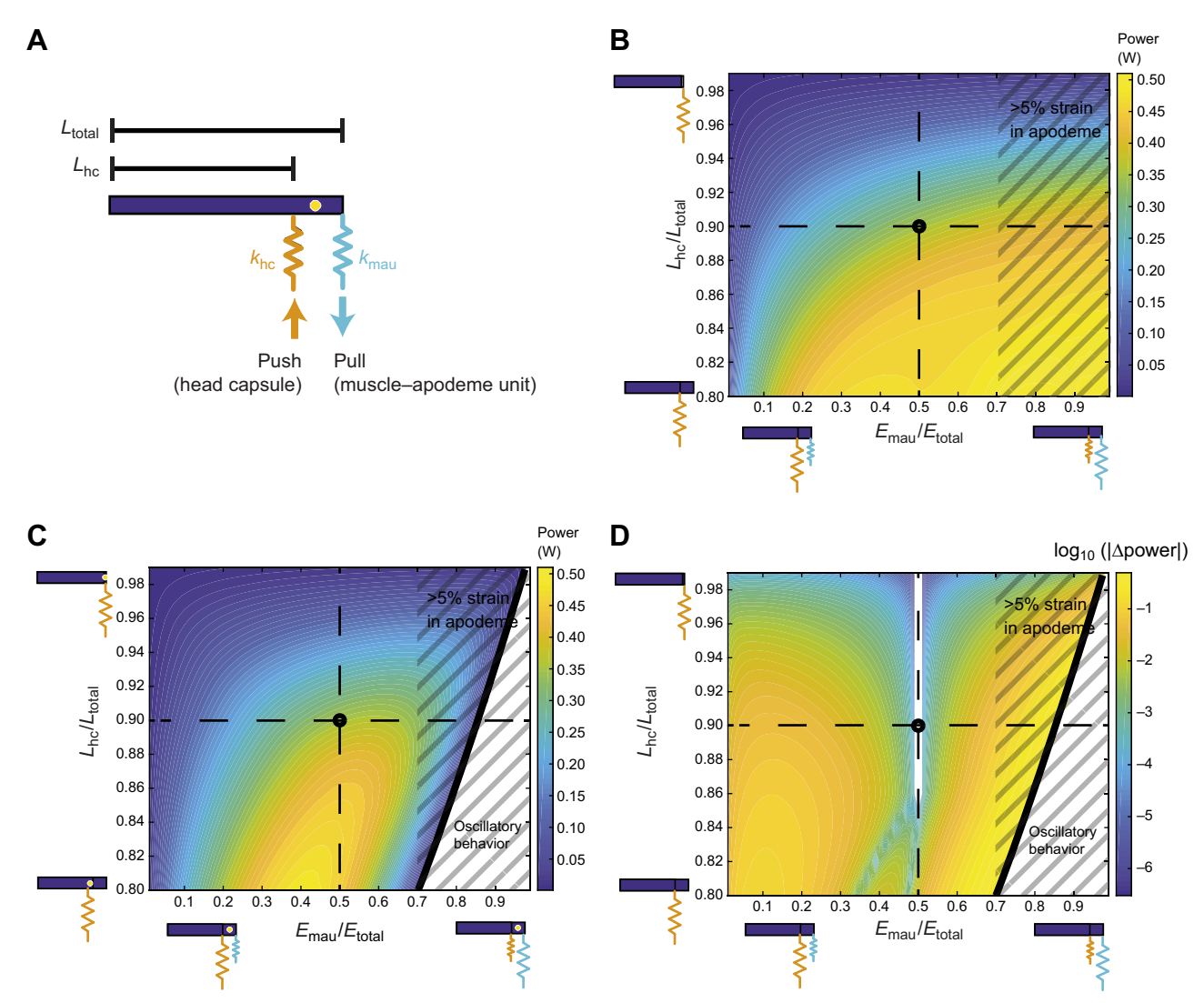


Fig. 7. Simulations of mandible and spring dynamics reveal that precise circular movement is possible with or without a constrained pin joint when the energy is partitioned equally between two springs. (A) The mandible is modeled as a thin, uniform rod that is actuated by a tensile spring pulling (muscle—apodeme unit) and compressive spring pushing (head capsule). The mandible can be mathematically constrained to a fixed pin joint (yellow circle). L_{total} , distance from the mandible tip to the tensile spring attachment point; L_{hc} , distance from the mandible tip to the compression spring attachment point (head capsule); k_{mau} , tensile spring constant of the muscle—apodeme unit; k_{hc} , compressive spring constant of the head capsule. (B) Translation and rotational dynamics (no fixed pin). The calculated power of the simulated mandible closure over the design space, varying the lever ratio ($L_{\text{hc}}/L_{\text{total}}$) and energy partition ($E_{\text{mau}}/E_{\text{total}}$). The black circle represents the *in vivo* configuration in which the head capsule spring is pushing at the location of the external attachment between the mandible and the head (located at 10% distally along the mandible length). (C) Rotation-only dynamics (fixed pin). When the simulation constrains the mandible movement to only rotational motion, the output map of the power changes relative to B, where the configurations in the white space do not show mandible closure in simulation. (D) The logarithm of the difference between the translation and rotation map in B and the rotation-only map in C reveals a narrow band (white space) where the power output is the same, because the mandibles close with the same dynamics whether or not a fixed pin joint is present. The spring schematics represent relative spring energy and are not meant to imply specific spring characteristics.

and the extensor apodeme (Bennet-Clark, 1975). A dual spring construction has been pointed out in the predatory strike of dragon fly larvae (Büsse et al., 2021). In the flea jump (Bennet-Clark and Lucey, 1967) and the froghopper jump (Burrows et al., 2008), energy storage has been found in exoskeletal structures (structures utilized similarly to the ant head deformation). Additional energy storage in the apodeme of flea and froghopper jumping muscles has not yet been ruled out, leaving open the possibility that both also use dual spring force couples.

Spring-driven engineered systems typically generate pure torques by storing and releasing energy via torsional springs, such as the EPFL jumper (Kovac et al., 2008), the MSU jumper (Zhao et al., 2013) and the locust-inspired robot (Zaitsev et al., 2015).

Implementation of dual spring force couples in synthetic systems would enable the design of tiny, space-limited, robots that can switch between using a LaMSA mechanism to generate ultrafast jumping rotations and a slower, multi-degrees of freedom, motor-driven mechanism for manipulating their environments, similar to the trap-jaw ant (Figs 1 and 2) (Zhang et al., 2020; Steinhardt et al., 2021).

Dual spring force couples reduce the need for joint constraints

In addition to defining the mechanism of force delivery to the mandibles, we also established that dual spring force couples reduce the need for joint constraints, such as pin joints. In general, joints

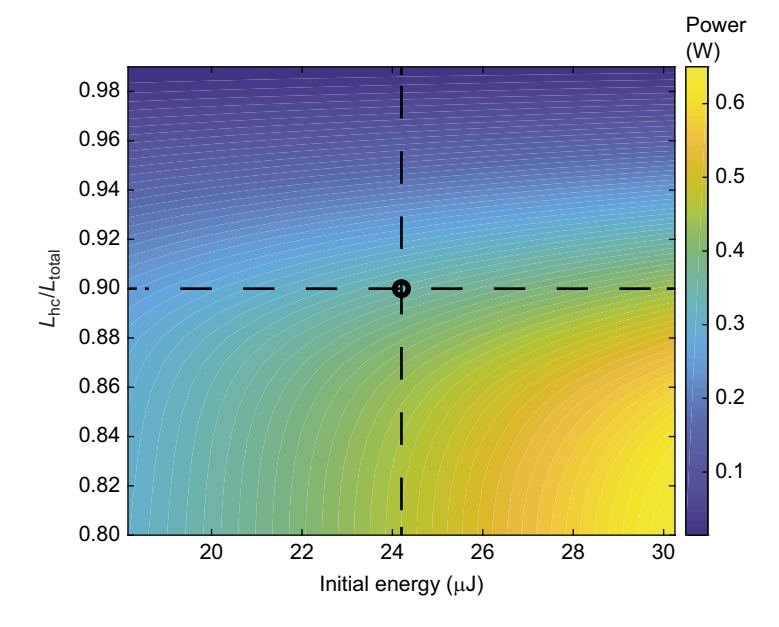


Fig. 8. A sensitivity analysis of energy and lever ratios yields uncertainty in power output that is within the range of the experimental dataset. A 10% uncertainty of the lever ratio at the initial energy of the strike exhibits a range of power outputs that are within 1 s.d. of the trap-jaw ant kinematics calculations (vertical dashed line). An uncertainty of 6 μJ across the modeled pivot position (horizontal dashed line) yields power outputs slightly outside 1 s.d., but within the range of observed power output calculated from trap-jaw kinematics.

both withstand dynamic loading from movement and overcome dissipative forces at the interface. In small, ultrafast rotating systems, these two factors limit the utility of joints. For example, in the case of pin joints (one degree of freedom kinematic pair that constrains the motion of one body to a planar rotation relative to the other), which are typically associated with precise rotational movements, the centrifugal force of the rotating body applies stress at the interface of the joint, while the dissipative forces at the interface remove energy, ultimately restrict speed and overall contribute to the wear and tear of joints. Yet, given the repeated-use and incredibly fast angular velocities of a trap-jaw ant mandible strike, typical constrained joint construction, such as found in pin joints, should be costly, if not unusable.

The rotational kinematics of trap-jaw ant mandibles may share some rotational and actuation principles with devil sticks (also called juggling sticks), which are simple, unconstrained beams with a center of rotation determined by the location of applied forces, rather than constrained pin joints. In these systems, forces are not applied at the point of rotation. However, if the applied forces were to cause a net force at the desired point of rotation, then the desired point of rotation needs to be constrained and must withstand the loads from the applied forces. Scaling juggling sticks down to the size of an ant mandible, applying zero net force to the point of rotation, and using spring recoil to generate 'pin like' kinematics is a viable and intriguing mechanism to minimize wear and tear at the joint. Moreover, it is not uncommon for ant mandibles to lack pin joint connections to the head: for example, the integration of scanning electron microscopy and µCT have shown that neither Protanilla lini nor Drylus helvolus mandibles have pin joints (Boudinot et al., 2021; Richter et al., 2021). Protanilla lini, however, has been hypothesized to be able to snap its jaws shut (Richter et al., 2021), and the placement of P. nilli's distal clypeal knob could cause recoil of the head to result in the same dual force coupling action observed in O. brunneus. Likewise, mantis shrimp and trap-jaw spiders lack a pin joint at the primary joint used for their rapid raptorial strikes (Patek et al., 2007; Wood, 2020).

Even though these dynamic simulations indicate that ultrafast, precise rotation can be achieved through dual spring force couples and without constrained pin joints, this still leaves open

the question of how the mandible-head joint is configured in trapjaw ants. Mandible joint morphology (Fig. 3) and multi-degrees of freedom, muscle-driven mandible manipulations by freely behaving ants (Fig. 1B) indicate a relatively unconstrained morphological attachment between the mandible and head. The proximal base of the mandible only contacts the head externally during the initial degrees of mandible rotation (Fig. 5A), congruent with the recoil displacement (Fig. 4), and kinematic transition to deceleration (Fig. 6). Moreover, post-strike mandible oscillations (Movie 1) reveal that the ant mandible is underdamped – demonstrating, again, that dissipation in the mandible joint is likely low as a result of few constraints.

Interpreting mandible joint morphology is challenged by the fact that prior studies and our morphological analyses are based on reconstruction and visualization of the joint and joint attachment in the non-spring-loaded head configuration; the spring-loaded system is characterized by a deformation of the entire head along with a muscle–apodeme loading on the medial edge of the mandible – both of which could yield a configuration and constraint that only exists when the head is loaded and deformed, and is not visible through these analyses. To visualize this configuration requires cryopreservation of a living, spring-loaded trap-jaw ant just prior to striking, which may be possible in future research with the necessary cryo-imaging capabilities and cooperative, living trapjaw ants. Even so, this type of unconstrained and transient joint is, by its very nature, not morphologically constrained and obvious [see Fig. 3 and the more detailed scanning electron micrographs in Gronenberg (1995a), which illustrate the simple joint morphology of a non-elastically loaded head]. Therefore, a combination of morphology, kinematics and modeling – as we have done here – is more likely to provide a conclusive pathway to establishing this mechanism.

This finding in trap-jaw ant mandibles stimulates further examination of the multi-functionality and stress reduction present in the diversity of other joint actuation mechanisms, and especially how organisms reduce friction in joint rotation at small scales. Locust LaMSA systems use a reinforced pin-type joint, most likely because they distribute spring energy such that the forces at the joint are almost zero (as the trap-jaw ant does) (Burrows, 2016). The locust leg is used for both jumping and kicking (Burrows, 1995);

these two behaviors have sufficiently different mass distributions that there would not be a single spring energy distribution that would minimize joint forces for both. Likewise, the effects of varying loading on spring energy distribution could be experimentally determined in snapping versus jaw-jumping trapjaw ants (Patek et al., 2006). Arthropod joint dynamics and morphology are highly diverse, including ball and socket, side-byside, uniform (Tajiri et al., 2011), screw (van de Kamp et al., 2011), geared (Burrows and Sutton, 2013), pin (Heitler, 1977; Burrows, 2016) and sliding joints (Patek, 2002; Kaji et al., 2018; Patek and Longo, 2018), as well as complex insect wing joints (Dudley, 2000; Hedenström, 2014; Gau et al., 2019).

This discovery of dual elastic energy storage, recoil and ultrafast rotational dynamics in trap-jaw ants applies to other ultrafast, small biological systems and has implications for precise motion in multifunctional robotics and tiny engineered systems such as MEMS (Park et al., 2016; St Pierre et al., 2020; Jiang and Gravish, 2021). Pin joints, in both biological and synthetic systems, are ultimately limited by their range of motion, dynamic forces and energetic losses at the interface (Nadein and Gorb, 2022). Pin joint range of motion is typically dictated by a design trade-off with forces applied to the moving body, as found in the planar silicon pin joints for MEMS (Contreras and Pister, 2016). In these designs, high forces on the moving body require more restrictive geometries that limit the range of motion. These pin joint forces can emerge from static loads as well as dynamic loads due to fast moving bodies. MEMS limit friction in rotational joints by using micro-ball bearings (Ghalichechian et al., 2008), hydro-dynamic bearings (Frechette et al., 2005), and air bearings created through magnetic suspensions (Wu et al., 2004) or on a liquid film (Takei et al., 2008; Chan et al., 2012). These devices achieve precise, kinematic rotations, but with top rotation frequencies of 60 rad s⁻¹ or less. Rotation rates of tens of thousands of rad s⁻¹ have been achieved with gas bearings (Fréchette et al., 2000; Livermore et al., 2004), which are, of course, impractical for biological systems as well as many engineered systems. Friction bearings in microrobot legs have successfully achieved clearance between the shaft and housing to minimize friction, but with a tradeoff between kinematic precision and rotational frequency (which could not exceed 630 rad s⁻¹) (St. Pierre et al., 2018). Another way to circumvent surface forces in joints is by using compliant mechanisms, which can offer precision motion through the deflection of flexural elements (Howell, 2013; Lau et al., 2014; Mountcastle et al., 2019), but with the limitation that the maximal elastic strain of flexural elements limits the range of achievable motion. To achieve a large range of motion, this limitation requires the use of high strain materials not commonly found in engineered systems or very large flexures.

Trap-jaw ant strikes show that the dissipative speed constraints seen in engineered small mechanical systems can be navigated by carefully distributed forces, such that rotation emerges from these forces alone. Appropriate force allocation between actuators (including springs) can thus be used as a substitute for kinematic constraints, with the resulting motion being precise and fast, while minimizing dissipation. Given the fast speeds and high range of motion of the mandible closure, a traditional pin joint is not necessary based on our discoveries of elastic energy allocation, may not even be feasible because of costly dissipation at these scales, and certainly would not be advisable given the need for multi-degrees of freedom muscle-driven movements when not using the LaMSA mechanism. Dual spring actuated, juggling stick-like dynamics in trap-jaw ant ultrafast strikes possibly evolved as a

critical feature that is likely widespread in biological LaMSA systems of this scale, and offers a strategy worth pursuing in synthetic LaMSA systems. The remarkable trap-jaw ant system has provided an answer to how precise, fast rotations can be achieved through the allocation of tiny, potent displacements of spring-based propulsion.

Appendix

Mathematical model derivation

The two degrees of freedom equations of motion for mandible closure are derived with respect to the coordinate frame located equidistant between the forces applied by the head capsule and the muscle—apodeme unit. For the right mandible, this is for a mandible rotating closed in a counterclockwise direction for a right-handed coordinate frame, and for the left mandible, it is for a mandible rotating closed in a clockwise rotation in a left-handed coordinate frame. The coordinate frame is shown for the right mandible in Fig. A1.

The equations are as follows:

$$m\frac{\mathrm{d}^2 y}{\mathrm{d}t^2} = F_{\mathrm{hc}} - F_{\mathrm{mau}} + mL_{\mathrm{cm}} \left(\frac{d\theta}{dt}\right)^2 \sin(\theta), \tag{A1}$$

$$I_{p} \frac{d^{2} \theta}{dt^{2}} = F_{hc} \left(\frac{L_{total} - L_{hc}}{2} \right) \cos(\theta) + F_{mau} \left(\frac{L_{total} - L_{hc}}{2} \right) \times \cos(\theta), \tag{A2}$$

where m is the mass of the mandible; $F_{\rm hc}$ and $F_{\rm mau}$ are the forces from the recoil of the head capsule spring and muscle—apodeme unit spring, respectively; $L_{\rm total}$, $L_{\rm hc}$ and $L_{\rm cm}$ are the total mandible length, the distance from the tip of the mandible to the head capsule spring, and the distance from the coordinate frame to the center of mass; and $I_{\rm p}$ is the mass moment of inertia of the mandible rotating about a point halfway between the attachment point of the two springs. The mass moment of inertia is calculated using the parallel axis theorem and is given generally as

$$I_{\rm p} = I + m(L_{\rm hc} - \frac{L_{\rm total}}{2} + \frac{L_{\rm total} - L_{\rm hc}}{2})^2,$$
 (A3)

where I is the mass moment of inertia of a slender rod rotating about the center of mass $(I=1/12mL_{\text{total}}^2)$.

The forces from the recoil of the springs are not constant and change as the mandible moves. The forces in each spring are the sum of the initial, translational and rotational displacements. For the force from the head capsule spring, a forward translation and the rotation of the mandible in the closing direction (counterclockwise for the right mandible) both result in a decrease in the force from the head capsule spring. Therefore, the force in the head capsule spring

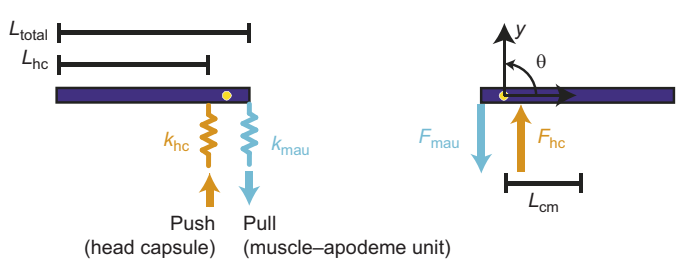


Fig. A1. The dynamic model of the mandible is derived for the left and right mandibles for a left-handed and right-handed coordinate system, respectively.

can be expressed as:

$$F_{\rm hc} = k_{\rm hc} \left(y_{\rm hc0} - y - \frac{L_{\rm total} - L_{\rm hc}}{2} \sin(\theta) \right). \tag{A4}$$

The force in the muscle-apodeme unit is expressed similarly. However, a forward translation results in the muscle-apodeme unit increasing in force, and the rotation of the mandible in the closing direction results in the muscle-apodeme unit decreasing in force:

$$F_{\text{mau}} = k_{\text{mau}} \left(y_{\text{mau0}} + y - \frac{L_{\text{total}} - L_{\text{hc}}}{2} \sin(\theta) \right). \tag{A5}$$

Therefore, the two equations of motion can be written in terms of the spring constants, displacements and distances:

$$m\frac{\mathrm{d}^{2}y}{\mathrm{d}t^{2}} = k_{\mathrm{hc}} \left(y_{\mathrm{hc0}} - y - \frac{L_{\mathrm{total}} - L_{\mathrm{hc}}}{2} \sin(\theta) \right)$$
$$- k_{\mathrm{mau}} \left(y_{\mathrm{mau0}} + y - \frac{L_{\mathrm{total}} - L_{\mathrm{hc}}}{2} \sin(\theta) \right)$$
$$+ mL_{\mathrm{cm}} \left(\frac{d\theta}{\mathrm{d}t} \right)^{2} \sin(\theta), \tag{A6}$$

$$\begin{split} I_{\rm p} \frac{\mathrm{d}^2 \theta}{\mathrm{d}t^2} = & \left(\frac{L_{\rm total} - L_{\rm hc}}{2} \right) \cos(\theta) \left(k_{\rm hc} \left(y_{\rm hc0} - y - \frac{L_{\rm total} - L_{\rm hc}}{2} \sin(\theta) \right) \right. \\ & \left. + k_{\rm mau} \left(y_{\rm mau0} + y - \frac{L_{\rm total} - L_{\rm hc}}{2} \sin(\theta) \right) \right). \end{split} \tag{A7}$$

Acknowledgements

We gratefully acknowledge Hongtao (Alex) Guo's help with data collection and Adrian Smith at the North Carolina Museum of Natural Sciences for help with ant collection and husbandry. We thank members of the Patek Lab and the MURI team for feedback and insights. This work was performed in part at the Duke University Shared Materials Instrumentation Facility (SMIF), a member of the North Carolina Research Triangle Nanotechnology Network (RTNN), which is supported by the National Science Foundation (award number ECCS-2025064) as part of the National Nanotechnology Coordinated Infrastructure (NNCI).

Competing interests

The authors declare no competing or financial interests.

Author contributions

Conceptualization: G.P.S., R.S., S.N.P.; Methodology: G.P.S., R.S., C.K., A.P.S., S.B., S.M.C., S.N.P.; Software: G.P.S., R.S.; Validation: G.P.S., S.N.P.; Formal analysis: G.P.S., R.S., S.N.P.; Investigation: G.P.S., R.S., C.K., A.P.S., S.N.P.; Resources: C.K., A.P.S., S.B., S.N.P.; Data curation: G.P.S., C.K., S.N.P.; Writing original draft: G.P.S., C.K., S.N.P.; Writing - review & editing: G.P.S., R.S., C.K., A.P.S., S.B., S.M.C., S.N.P.; Visualization: C.K., A.P.S., S.M.C., S.N.P.; Supervision: S.N.P.; Project administration: S.N.P.; Funding acquisition: G.P.S., A.P.S., S.B., S.N.P.

Funding

This research was supported by the U.S. Army Research Laboratory and the U.S. Army Research Office under contract/grant number W911NF-15-1-0358 (G.P.S., R.S., C.K., S.B., S.C., S.N.P.); the Royal Society (UF120507) and the UK Medical Research Council (MR/T046619/1) as part of the NSF/CIHR/DFG/FRQ/UKRI-MRC Next Generation Networks for Neuroscience Program to G.P.S.; and the Keohane Fellowship to A.P.S. while at Duke University and University of North Carolina Chapel Hill.

Data availability

Summary biological data are given in Table 1. The raw high speed videos are too large for repositories and are freely available upon request to the Patek Lab. The raw digitizing data and code are available from Dryad (Patek et al., 2022): https://doi.org/10.5061/dryad.c2fqz61bs.

References

- Aerts, P. (1998). Vertical jumping in Galago senegalensis: the quest for an obligate power amplifier. Philos. Trans. R. Soc. Lond. B 353, 1607-1620. doi:10.1098/rstb. 1998.0313
- Alexander, R. M. and Bennet-Clark, H. C. (1977). Storage of elastic strain energy in muscle and other tissues. *Nature* **265**, 114-117. doi:10.1038/265114a0
- Askew, G. N. and Marsh, R. L. (2001). The mechanical power output of the pectoralis muscle of blue-breasted quail (*Coturnix chinensis*): the *in vivo* length cycle and its implications for muscle performance. *J. Exp. Biol.* 204, 3587-3600. doi:10.1242/jeb.204.21.3587
- Askew, G. N. and Marsh, R. L. (2002). Muscle designed for maximum short-term power output: quail flight muscle. J. Exp. Biol. 205, 2153-2160. doi:10.1242/jeb. 205.15.2153
- Astley, H. C. and Roberts, T. J. (2014). The mechanics of elastic loading and recoil in anuran jumping. *J. Exp. Biol.* **217**, 4372-4378. doi:10.1242/jeb.110296
- Bennet-Clark, H. C. (1975). The energetics of the jump of the locust Schistocerca gregaria. J. Exp. Biol. 63, 53-83. doi:10.1242/jeb.63.1.53
- Bennet-Clark, H. C. and Lucey, E. C. A. (1967). The jump of the flea: A study of the energetics and a model of the mechanism. *J. Exp. Biol.* **47**, 59-76. doi:10.1242/jeb.47.1.59
- Bolmin, O., Wei, L., Hazel, A. M., Dunn, A. C., Wissa, A. and Alleyne, M. (2019). Latching of the click beetle (Coleoptera: Elateridae) thoracic hinge enabled by the morphology and mechanics of conformal structures. *J. Exp. Biol.* 222, jeb196683. doi:10.1242/jeb.196683
- Bolmin, O., Socha, J. J., Alleyne, M., Dunn, A. C., Fezzaa, K. and Wissa, A. A. (2021). Nonlinear elasticity and damping govern ultrafast dynamics in click beetles. *Proc. Natl. Acad. Sci. USA* 118, e2014569118. doi:10.1073/pnas. 2014569118
- Boudinot, B. E., Moosdorf, O. T. D., Beutel, R. G. and Richter, A. (2021). Anatomy and evolution of the head of *Dorylus helvolus* (Formicidae: Dorylinae): Patterns of sex- and caste-limited traits in the sausagefly and the driver ant. *J. Morphol.* 282, 1616-1658. doi:10.1002/jmor.21410
- **Burrows, M.** (1995). Motor patterns during kicking movements in the locust. *J. Comp. Physiol. A* **176**, 289-305. doi:10.1007/BF00219055
- Burrows, M. (2016). Development and deposition of resilin in energy stores for locust jumping. J. Exp. Biol. 219, 2449-2457. doi:10.1242/jeb.138941
- Burrows, M. and Sutton, G. P. (2013). Interacting gears synchronize propulsive leg movements in a jumping insect. *Science* **341**, 1254-1256. doi:10.1126/science.
- Burrows, M., Shaw, S. and Sutton, G. (2008). Resilin and chitinous cuticle form a composite structure for energy storage in jumping by froghopper insects. BMC Biol. 6, 1-16. doi:10.1186/1741-7007-6-41
- Büsse, S., Koehnsen, A., Rajabi, H. and Gorb, S. N. (2021). A controllable dual-catapult system inspired by the biomechanics of the dragonfly larvae's predatory strike. Sci. Robot. 6, eabc8170. doi:10.1126/scirobotics.abc8170
- Chan, M. L., Yoxall, B., Park, H., Kang, Z., Izyumin, I., Chou, J., Megens, M. M., Wu, M. C., Boser, B. E. and Horsley, D. A. (2012). Design and characterization of MEMS micromotor supported on low friction liquid bearing. *Sens. Actuator A Phys.* 177, 1-9. doi:10.1016/j.sna.2011.08.003
- Contreras, D. S. and Pister, K. S. J. (2016). Durability of silicon pin-joints for microrobotics. 2016 International Conference on Manipulation, Automation and Robotics at Small Scales (MARSS).
- Dai, Z., Min, Y. and Gorb, S. N. (2006). Frictional characteristics of the beetle headjoint material. Wear 260, 168-174. doi:10.1016/j.wear.2004.12.042
- Dickinson, M. (2006). Insect flight. Curr. Biol. 16, R309-R314. doi:10.1016/j.cub. 2006.03.087
- Dudley, R. (2000). The Biomechanics of Insect Flight: Form, Function, Evolution. Princeton, NJ, USA: Princeton University Press.
- Fedorov, A., Beichel, R., Kalpathy-Cramer, J., Finet, J., Fillion-Robin, J.-C., Pujol, S., Bauer, C., Jennings, D., Fennessy, F., Sonka, M. et al. (2012). 3D Slicer as an image computing platform for the Quantitative Imaging Network. *Magn. Reson. Imaging* **30**, 1323-1341. doi:10.1016/j.mri.2012.05.001
- Fréchette, L. G., Jacobson, S. A., Breuer, K. S., Ehrich, F. F., Ghodssi, R., Khanna, R., Wong, C. W., Zhang, X., Schmidt, M. A., Epstein, A. H. (2000). Demonstration of a microfabricated high-speed turbine supported on gas bearings. Solid-State Sensor and Actuator Workshop, Hilton Head Island, South Carolina, USA. pp. 43-47.
- Frechette, L. G., Jacobson, S. A., Breuer, K. S., Ehrich, F. F., Ghodssi, R., Khanna, R., Chee Wei, W., Xin, Z., Schmidt, M. A. and Epstein, A. H. (2005). High-speed microfabricated silicon turbomachinery and fluid film bearings. *J. Microelectromech. Syst.* 14, 141-152. doi:10.1109/JMEMS.2004.839008
- Galantis, A. and Woledge, R. (2003). The theoretical limits to the power output of a muscle–tendon complex with inertial and gravitational loads. *Proc. R. Soc. B* 270, 1493-1498. doi:10.1098/rspb.2003.2403
- Garcia, M., Kuo, A., Peattie, A., Wang, P. and Full, R. J. (2000). Damping and size: insights and biological inspiration. International Symposium on Adaptive Motion of Animals and Machines. McGill University.
- Gau, J., Gravish, N. and Sponberg, S. (2019). Indirect actuation reduces flight power requirements in *Manduca sexta* via elastic energy exchange. *J. R. Soc. Interface* 16, 20190543. doi:10.1098/rsif.2019.0543

- Gau, J., Gemilere, R., Fm Subteam, L.-V., Lynch, J., Gravish, N. and Sponberg, S. (2021). Rapid frequency modulation in a resonant system: aerial perturbation recovery in hawkmoths. *Proc. R. Soc. B* 288, 20210352. doi:10.1098/rspb.2021. 0352
- Ghalichechian, N., Modafe, A., Beyaz, M. I. and Ghodssi, R. (2008). Design, fabrication, and characterization of a rotary micromotor supported on microball bearings. J. Microelectromech. Syst. 17, 632-642. doi:10.1109/JMEMS.2008. 916346
- **Gronenberg, W.** (1995a). The fast mandible strike in the trap-jaw ant *Odontomachus* I. Temporal properties and morphological characteristics. *J. Comp. Physiol. A* **176**, 391-398. doi:10.1007/BF00219064
- **Gronenberg, W.** (1995b). The fast mandible strike in the trap-jaw ant *Odontomachus*. II. Motor control. *J. Comp. Physiol. A* **176**, 399-408. doi:10. 1007/BF00219065
- Gronenberg, W. (1996). Fast actions in small animals: springs and click mechanisms. J. Comp. Physiol. A 178, 727-734. doi:10.1007/BF00225821
- Hedenström, A. (2014). How insect flight steering muscles work. PLoS Biol. 12, e1001822. doi:10.1371/journal.pbio.1001822
- Heitler, W. J. (1977). The locust jump: III. Structural specializations of the metathoracic tibiae. *J. Exp. Biol.* **67**, 29-36. doi:10.1242/jeb.67.1.29
- Howell, L. L. (2013). Compliant mechanisms. In 21st Century Kinematics (ed. J. McCarthy), pp. 189-216. London: Springer.
- Ilton, M., Bhamla, M. S., Ma, X., Cox, S. M., Fitchett, L. L., Kim, Y., Koh, J.-s., Krishnamurthy, D., Kuo, C.-Y., Temel, F. Z. et al. (2018). The principles of cascading power limits in small, fast biological and engineered systems. *Science* 360, eaao1082. doi:10.1126/science.aao1082
- Ilton, M., Cox, S. M., Egelmeers, T., Sutton, G. P., Patek, S. N. and Crosby, A. J. (2019). The effect of size-scale on the kinematics of elastic energy release. *Soft Mat.* 15, 9579-9586. doi:10.1039/C9SM00870E
- Jiang, M. and Gravish, N. (2021). Reconfigurable laminates enable multifunctional robotic building blocks. Smart Mater. Struct. 30, 035005. doi:10.1088/1361-665X/ abdc3f
- Jorge, J. F., Bergbreiter, S. and Patek, S. N. (2021). Pendulum-based measurements reveal impact dynamics at the scale of a trap-jaw ant. *J. Exp. Biol.* **224**, jeb232157. doi:10.1242/jeb.232157
- Kaji, T., Anker, A., Wirkner, C. S. and Palmer, A. R. (2018). Parallel saltational evolution of ultrafast movements in snapping shrimp claws. *Curr. Biol.* 28, 106-113.e4. doi:10.1016/j.cub.2017.11.044
- Kovac, M., Fuchs, M., Guignard, A., Zufferey, J. C. and Floreano, D. (2008). A miniature 7g jumping robot. In 2008 leee International Conference on Robotics and Automation, Vols 1-9, pp. 373-378. New York: IEEE.
- Kuan, K.-C., Chiu, C.-I., Shih, M.-C., Chi, K.-J. and Li, H.-F. (2020). Termite's twisted mandible presents fast, powerful, and precise strikes. Sci. Rep. 10, 9462. doi:10.1038/s41598-020-66294-1
- Larabee, F. J., Gronenberg, W. and Suarez, A. V. (2017). Performance, morphology and control of power-amplified mandibles in the trap-jaw ant *Myrmoteras* (Hymenoptera: Formicidae). *J. Exp. Biol.* 220, 3062-3071. doi:10. 1242/jeb.156513
- Larabeé, F. J., Smith, A. A. and Suarez, A. V. (2018). Snap-jaw morphology is specialized for high-speed power amplification in the Dracula ant, *Mystrium camillae*. R. Soc. Open Sci. 5, 181447, doi:10.1098/rsos.181447
- Lau, G.-K., Chin, Y.-W., Goh, J. T.-W. and Wood, R. J. (2014). Dipteran-insectinspired thoracic mechanism with nonlinear stiffness to save inertial power of flapping-wing flight. *IEEE Trans. Robot.* 30, 1187-1197. doi:10.1109/TRO.2014. 2333112
- Lieber, R. L., Leonard, M. E., Brown, C. G. and Trestik, C. L. (1991). Frog semitendinosis tendon load-strain and stress-strain properties during passive loading. Am. J. Physiol. 261, C86-C92. doi:10.1152/ajpcell.1991.261.1.C86
- Livermore, C., Forte, A. R., Lyszczarz, T., Umans, S. D., Ayon, A. A. and Lang, J. H. (2004). A high-power MEMS electric induction motor. *J. Microelectromech.* Syst. 13, 465-471. doi:10.1109/JMEMS.2004.828736
- Longo, S. J., Cox, S. M., Azizi, E., Ilton, M., Olberding, J. P., St. Pierre, R. and Patek, S. N. (2019). Beyond power amplification: Latch-mediated spring actuation is an emerging framework for the study of diverse elastic systems. *J. Exp. Biol.* **222**, jeb197889. doi:10.1242/jeb.197889
- Longo, S. J., Ray, W., Farley, G. M., Harrison, J., Jorge, J., Kaji, T., Palmer, A. R. and Patek, S. N. (2021). Snaps of a tiny amphipod push the boundary of ultrafast, repeatable movement. *Curr. Biol.* 31. R116-R117. doi:10.1016/j.cub.2020.12.025
- Matsuda, A., Aonuma, H. and Kaneko, S. i. (2020). A structural analysis based on kinetic model of trap-jaw in *Odontomachus*. Proceedings of the Seventh Asia International Symposium on Mechatronics (ed. B. Duan, K. Umeda and W. Hwang), pp. 289-294. Singapore: Science Press.
- McHenry, M. J., Anderson, P. S. L., Van Wassenbergh, S., Matthews, D. G., Summers, A. P. and Patek, S. N. (2016). The comparative hydrodynamics of rapid rotation by predatory appendages. *J. Exp. Biol.* 219, 3399-3411. doi:10. 1242/jeb.140590
- Miyan, J. A., Ewing, A. W. and Lighthill, M. J. (1985). How Diptera move their wings: a re-examination of the wing base articulation and muscle systems concerned with flight. *Philos. Trans. R. Soc. Lond. B Biol. Sci.* 311, 271-302. doi:10.1098/rstb.1985.0154

- Moo, E. K., Peterson, D. R., Leonard, T. R., Kaya, M. and Herzog, W. (2017). In vivo muscle force and muscle power during near-maximal frog jumps. *PLoS One* 12, e0173415. doi:10.1371/journal.pone.0173415
- Mountcastle, A. M., Helbling, E. F. and Wood, R. J. (2019). An insect-inspired collapsible wing hinge dampens collision-induced body rotation rates in a microrobot. J. R. Soc. Interface 16, 20180618. doi:10.1098/rsif.2018.0618
- Nadein, K. and Gorb, S. (2022). Lubrication in the joints of insects (Arthropoda: Insecta). J. Zool. 316, 24-39. doi:10.1111/jzo.12922
- Nüchter, T., Benoit, M., Engel, U., Özbek, S. and Holstein, T. W. (2006). Nanosecond-scale kinetics of nematocyst discharge. Curr. Biol. 16, R316-R318. doi:10.1016/i.cub.2006.03.089
- Park, Y.-J., Lee, J.-G., Jeon, S., Ahn, H., Koh, J., Ryu, J., Cho, M. and Cho, K.-J. (2016). Dual-stiffness structures with reconfiguring mechanism: design and investigation. J. Intell. Mater. Syst. Struct. 27, 995-1010. doi:10.1177/1045389X15577642
- Patek, S. (2002). Squeaking with a sliding joint: mechanics and motor control of sound production in palinurid lobsters. J. Exp. Biol. 205, 2375-2385. doi:10.1242/ jeb.205.16.2375
- Patek, S. N. and Longo, S. J. (2018). Evolutionary biomechanics: the pathway to power in snapping shrimp. *Curr. Biol.* 28, R115-R117. doi:10.1016/j.cub.2017.12. 033
- Patek, S. N., Baio, J. E., Fisher, B. F. and Suarez, A. V. (2006). Multifunctionality and mechanical origins: ballistic jaw propulsion in trap-jaw ants. *Proc. Natl. Acad.* Sci. USA 103, 12787-12792. doi:10.1073/pnas.0604290103
- Patek, S. N., Nowroozi, B. N., Baio, J. E., Caldwell, R. L. and Summers, A. P. (2007). Linkage mechanics and power amplification of the mantis shrimp's strike. J. Exp. Biol. 210, 3677-3688. doi:10.1242/jeb.006486
- Patek, S. N., Dudek, D. M. and Rosario, M. V. (2011). From bouncy legs to poisoned arrows: elastic movements in invertebrates. *J. Exp. Biol.* **214**, 1973-1980. doi:10.1242/jeb.038596
- Patek, S. N., Rosario, M. V. and Taylor, J. R. A. (2013). Comparative spring mechanics in mantis shrimp. J. Exp. Biol. 215, 1317-1329. doi:10.1242/jeb. 078998
- Patek, S. N. et al. (2022). Dual spring force couples yield multifunctionality and ultrafast, precision rotation in tiny biomechanical systems. *Dryad*, *Dataset*. doi:10. 5061/dryad.c2fqz61bs
- Richter, A., Hita Garcia, F., Keller, R. A., Billen, J., Katzke, J., Boudinot, B. E., Economo, E. P. and Beutel, R. G. (2021). The head anatomy of *Protanilla lini* (Hymenoptera: Formicidae: Leptanillinae), with a hypothesis of their mandibular movement. *Myrmecol. News* **31**, 85-114.
- Roberts, T. J. and Azizi, E. (2011). Flexible mechanisms: the diverse roles of biological springs in vertebrate movement. *J. Exp. Biol.* **214**, 353-361. doi:10. 1242/jeb.038588
- Rosario, M. D. (2015). Biomechanics of Hierarchical Elastic Systems. *PhD thesis*, Duke University.
- Rosario, M. V. and Patek, S. N. (2015). Multi-level analysis of elastic morphology: the mantis shrimp's spring. J. Morphol. 276, 1123-1135. doi:10.1002/jmor.20398
- Rosario, M. V., Sutton, G. P., Patek, S. N. and Sawicki, G. S. (2016). Muscle–spring dynamics in time-limited, elastic movements. *Proc. R. Soc. B* 283, 20161561. doi:10.1098/rspb.2016.1561
- Scherge, M. (2001). Scale dependence of friction. Proceedings of the Second World Tribology Conference. Vienna, Austria.
- Schindelin, J., Arganda-Carreras, I., Frise, E., Kaynig, V., Longair, M., Pietzsch, T., Preibisch, S., Rueden, C., Saalfeld, S., Schmid, B. et al. (2012). Fiji: an open-source platform for biological-image analysis. *Nat. Methods* 9, 676-682. doi:10.1038/nmeth.2019
- Snedeker, J. G. and Foolen, J. (2017). Tendon injury and repair a perspective on the basic mechanisms of tendon disease and future clinical therapy. *Acta Biomater.* **63**, 18-36. doi:10.1016/j.actbio.2017.08.032
- Spagna, J. C., Vakis, A. I., Schmidt, C. A., Patek, S. N., Zhang, X., Tsutsui, N. D. and Suarez, A. V. (2008). Phylogeny, scaling, and the generation of extreme forces in trap-jaw ants. *J. Exp. Biol.* 211, 2358-2368. doi:10.1242/jeb. 015263
- St. Pierre, R., Gosrich, W. and Bergbreiter, S. (2018). A 3D-printed 1 mg legged microrobot running at 15 body lengths per second. Solid-State Sensors, Actuators and Microsystems Workshop, pp. 59-62. Hilton Head, South Carolina, USA
- St Pierre, R., Gao, W., Clark, J. E. and Bergbreiter, S. (2020). Viscoelastic legs for open-loop control of gram-scale robots. *Bioinspir. Biomim.* **15**, 055005. doi:10. 1088/1748-3190/ab9fa9
- Steinhardt, E., Hyun, N. P., Koh, J., Freeburn, G., Rosen, M. H., Temel, F. Z., Patek, S. N. and Wood, R. J. (2021). A physical model of mantis shrimp for exploring the dynamics of ultra-fast systems. *Proc. Natl. Acad. Sci. USA* 118, e2026833118. doi:10.1073/pnas.2026833118
- Sutton, G. P., Mendoza, E., Azizi, E., Longo, S. J., Olberding, J. P., Ilton, M. and Patek, S. N. (2019). Why do large animals never actuate their jumps with latch-mediated springs? Because they can jump higher without them. *Integr. Comp. Biol.* 145, 1-10. doi:10.1093/icb/icz145
- Tajiri, R., Misaki, K., Yonemura, S. and Hayashi, S. (2011). Joint morphology in the insect leg: evolutionary history inferred from *Notch* loss-of-function

- phenotypes in *Drosophila*. *Development* **138**, 4621-4626. doi:10.1242/dev. 067330
- Takei, A., Binh-Khiem, N., Iwase, E., Matsumoto, K. and Shimoyama, I. (2008). Liquid motor driven by electrowetting. 2008 IEEE 21st International Conference on Micro Electro Mechanical Systems 2008, pp. 42-45. doi:10.1109/MEMSYS.2008. 4443588
- **Trimmer, W. S. N.** (1989). Microrobots and micromechanical systems. *Sens. Actuators* **19**, 267-287. doi:10.1016/0250-6874(89)87079-9
- van de Kamp, T., Vagovič, P., Baumbach, T. and Riedel, A. (2011). A biological screw in a beetle's leg. *Science* 333, 52-52. doi:10.1126/science.1204245
- Walker, S. M., Thomas, A. L. R. and Taylor, G. K. (2012). Operation of the alula as an indicator of gear change in hoverflies. J. R. Soc. Interface 9, 1194-1207. doi:10. 1098/rsif.2011.0617
- Walker, S. M., Schwyn, D. A., Mokso, R., Wicklein, M., Müller, T., Doube, M., Stampanoni, M., Krapp, H. G. and Taylor, G. K. (2014). In vivo time-resolved microtomography reveals the mechanics of the blowfly flight motor. *PLoS Biol.* 12, e1001823. doi:10.1371/journal.pbio.1001823

- Wood, H. M. (2020). Morphology and performance of the 'trap-jaw' cheliceral strikes in spiders (Araneae, Mecysmaucheniidae). J. Exp. Biol. 223, jeb219899. doi:10. 1242/ieb.219899
- Wu, X.S., Chen, W.-Y., Zhao, X.-L. and Zhang, W.-P. (2004). Micromotor with electromagnetically levitated rotor using separated coils. *Electron. Lett.* 40, 1-2
- Zaitsev, V., Gvirsman, O., Ben Hanan, U., Weiss, A., Ayali, A. and Kosa, G. (2015). A locust-inspired miniature jumping robot. *Bioinspir. Biomim.* 10, 066012. doi:10.1088/1748-3190/10/6/066012
- Zhang, C., Zou, W., Ma, L. and Wang, Z. (2020). Biologically inspired jumping robots: a comprehensive review. *Robot. Auton. Syst.* **124**, 103362. doi:10.1016/j. robot.2019.103362
- Zhao, J., Xu, J., Gao, B., Xi, N., Cintrón, F. J., Mutka, M. W. and Xiao, L. (2013). MSU jumper: a single-motor-actuated miniature steerable jumping robot. *IEEE Trans. Robot.* **29**, 602-614. doi:10.1109/TRO.2013.2249371